Ice Shape Classification for Swept Wings

Michael B. Bragg[1] and William Yoshida[2]
University of Washington, Seattle, Washington, 98195, USA

Andy P. Broeren[3]
NASA John H. Glenn Research Center, Cleveland, Ohio, 44135, USA

Sam Lee[4]
HX5, LLC, Cleveland, Ohio, 44135, USA

Brian S. Woodard[5]
University of Illinois at Urbana-Champaign, Urbana, Illinois, 61801, USA

An important consideration for swept-wing ice shapes is the level of geometric fidelity required to accurately capture the aerodynamics. One way to help make the task of addressing this more manageable is to organize the ice shapes into a small number of classifications. These classifications are done by grouping similar ice shape geometries that also have similar iced wing aerodynamics. Ice shape classifications for airfoils are more mature and are reviewed as an example. Swept-wing ice shape classifications are based on the well-established airfoil classifications and here five classifications are proposed: leading-edge roughness, streamwise ice, 3D leading-edge horn, highly 3D leading-edge horn and spanwise ridge. Recent data on swept-wing icing aerodynamics is used to develop and support this classification. The development, or suppression, of the leading-edge separation vortex on swept wings without a leading-edge device is seen to be key in the classification of the highly 3D leading-edge horn.

I. Introduction

Understanding the effects of ice accretion on the aerodynamic performance of large-scale, swept wings is an important consideration affecting the design and certification of transport

---

[1] Frank and Julie Jungers Dean Emeritus, College of Engineering, and Professor Emeritus, William E. Boeing Department of Aeronautics and Astronautics, University of Washington; Room 211, Guggenheim Hall, Box 352400, AIAA fellow.
[2] Graduate Research Assistant, William E. Boeing Department of Aeronautics and Astronautics, University of Washington; Room 211, Guggenheim Hall, Box 352400.
[3] Research Aerospace Engineer, Icing Branch, 21000 Brookpark Rd., MS 11-2, Associate Fellow AIAA.
[4] Engineer V, Icing Branch, 21000 Brookpark Rd., MS 11-2, Senior Member AIAA.
[5] Research Associate, Dept. of Aerospace Engineering, 306 Talbot Lab, 104 S. Wright St., Member AIAA.

aircraft. These effects on highly three-dimensional wings are currently not well documented and can present a significant challenge to airframe manufacturers, certification authorities, and research organizations. A large collaborative research program led by NASA, the Office National d'Etudes et Recherches Aérospatiales (ONERA), and the Federal Aviation Administration (FAA) is addressing these challenges. Broeren et al. [1] describe the objectives of this project in more detail. Two of the primary goals involve creating a database of realistic publicly available, swept-wing ice accretions and documenting the aerodynamics of the iced swept-wing configurations.

In the early stages of this research project an effort was made to classify swept-wing ice accretions by aerodynamic effect to organize and simplify the aerodynamic and ice accretion research.[2] However, the limited data on swept wings with ice accretions hampered the ability of the researchers to fully develop the classifications. Bragg et al.[3] reviewed the research on airfoil icing aerodynamics and classified ice accretions by their basic geometry and aerodynamics. This was made possible by the extensive past research into the aerodynamic performance effects and flowfield physics of ice accretions on airfoils and straight wings. However, swept wings with ice accretions have extremely complex geometry. Many icing conditions result in highly three-dimensional ice accretions that are often referred to as "scallops" or "lobster tails" due to their appearance and the complex spanwise variations in the ice geometry.[4] The aerodynamics of swept wings with ice accretions is also highly three dimensional and these effects must be considered in any swept-wing ice shape classification system.

A major issue, and one that will benefit significantly from swept-wing ice shape classification, is the level of geometric fidelity required to accurately capture the aerodynamics of these ice shapes. An ice accretion database for large-scale swept wings has been created based on a series of tests in the Icing Research Tunnel (IRT) at the NASA Glenn Research Center.[5] Thus, the effort to develop a swept-wing ice shape classification system relies heavily on the ice accretions measured in the IRT and tested with varying fidelity as artificial ice shapes in a series of aerodynamic wind tunnel tests in dry-air wind tunnels. The ice accretion database and the aerodynamic wind tunnel models are all based on the Common Research Model (CRM).[6-9] For this project, the full-scale geometry is a 65% scale version of the CRM, here referred to as the CRM65.[1] The design of the icing wind tunnel models is described by Fujiwara et al.[10] Low-Reynolds number testing was performed using an 8.9% scale model of the CRM65, and the high-Reynolds number testing utilized a 13.3% scale model. Broeren et al.,[11] Camello et al.,[12] and

Lum et al.[13] have presented results related to the low-Reynolds number aerodynamic testing with Camello et al. making a preliminary investigation into the ice shape fidelity effects relating to the aerodynamics. Papers by Broeren et al.,[14] Lee et al.,[15] Sandu et al.,[16] Woodard et al.[17] provide additional details regarding other aspects of these wind tunnel tests.

The purpose of this paper is to review and update the initial swept-wing ice shape classifications made by Broeren et al.[2] based on our more recent data and improved understanding. After reviewing the airfoil icing classifications, and the initial swept wing icing classifications, more recent data will be examined and used to update the current classifications. In addition, suggestions toward developing a more complete system will be presented including its limitations and challenges.

II. Background

Aerospace professionals usually think of ice shapes in terms of the accretion process. Labels such as rime ice, glaze ice, mixed accretions, etc. are often used. These labels are extremely useful when the objective is to understand or document the ice accretion on an aircraft. However, aircraft performance and safety in icing conditions depend primarily on the aerodynamics of the iced surfaces (lift, drag, moments, etc.) and these depend on the flowfield physics. Hence it is useful to classify ice shapes into a small set of shapes based on real ice accretion geometries considering their effect on the flowfield physics which govern the aerodynamics. This allows for iced surface aerodynamics to be studied and understood for a smaller, simplified, number of shapes which can be varied parametrically, and thus the aerodynamics better understood. Understanding these sensitivities can help engineers design ice simulations of reduced geometric fidelity and complexity that mimic the actual ice or a high-fidelity simulation.

Aircraft icing researchers and engineers often discuss ice shape fidelity using the phrase, “How good is good enough.” By this it is usually meant how accurately must the ice shape geometry be predicted by a computer code, or simulated for a wind tunnel or flight test, to generate sufficiently accurate aerodynamics for design or certification uses. How good is good enough first requires an answer to the question “good enough for what purpose?” The level of ice shape fidelity required for a specific research purpose, versus an aircraft certification action or aircraft design analysis may be different. Thus, a more general question might be “what is the effect of the level of fidelity on the iced wing aerodynamics?” Being able to reduce the problem to the study of the sensitivity of the key geometric features for swept wing ice shape classifications greatly facilitates addressing "How good is good enough," for swept wing ice shape prediction and simulation.

This section of the paper will describe the airfoil ice shape classification and as an example present a parametric study that has helped improve our understanding of iced-airfoil aerodynamics and the sensitivity of the aerodynamics to changes in geometry. Following the airfoil discussion, swept-wing ice shape classification is discussed.

A. Iced-Airfoil Classifications

Four ice shape classifications were identified and presented as part of the iced airfoil aerodynamics review paper by Bragg, et al.[3] These classifications were then used to help understand the relationship between airfoil design and iced airfoil aerodynamics, determine the critical ice shape geometric features, and their sensitivity on airfoil aerodynamics. The classifications were also useful to help understand iced airfoil flowfield physics and to address the level of fidelity needed to reproduce iced airfoil effects ("how good is good enough").

The development of the airfoil ice shape classifications followed these steps:

1. Reviewed all the different ice shapes and aerodynamic and flowfield effects observed from the many aerodynamic studies available on simulations of measured ice accretion shapes,
2. Grouped similar shapes that produced similar aerodynamic and flowfield effects,
3. Developed four airfoil ice shape classifications,
4. For each classification established the key flowfield features and the key geometric parameters that governed these effects,
5. Developed the sensitivity of the aerodynamic performance and flowfield features to these geometric parameters.

The classification development process and its application are depicted in Fig. 1. The Ice "Accretion Shapes" box depicts step 1 from above – Gather and review all available airfoil ice accretion shapes. The transition then from this box to the "2D Classification" box represents steps 2 and 3 where these accretion-based shapes were grouped and classified into common geometries with similar aerodynamics. Step 4 is represented in the "Critical geometric parameters" box where some of the most important geometric parameters of each classification is identified. The final box in the lower left then represents the many experiments and studies that have developed the sensitivity of airfoil aerodynamics to these geometric parameters for each classification. It is important to understand that this sensitivity depends on the airfoil design as represented by its

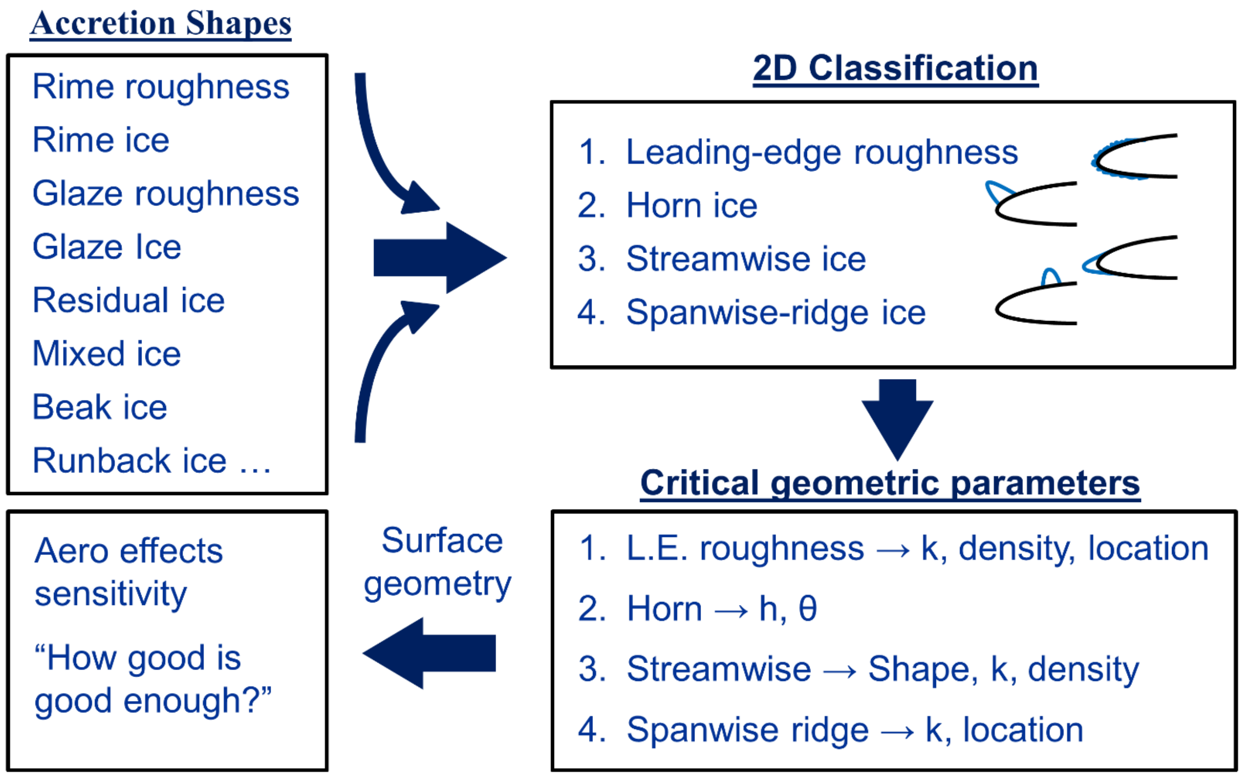

Fig. 1 Airfoil Ice Shape Classification Process

geometry. Thus, the airfoil surface geometry is important to include and is noted on the figure. While Reynolds number and Mach number sensitivity of iced airfoils are usually small,[3] it should also be a consideration for any application.

One example of the classification process that is included in Fig.1 is iced airfoil leading-edge roughness. Leading-edge roughness can result from many different ice accretion processes and from ice protection system operation. Initial accretions of rime and glaze ice result in leading-edge roughness. Residual ice left on a leading edge after ice protection system operation can also result in surface roughness. While the accretion processes are different, aerodynamically the flowfield physics are essentially the same. The roughness, which is often larger than the local boundary-layer thickness, extracts momentum from the flow and contributes to early boundary-layer transition and separation. Thus, one of the airfoil ice shape classifications is airfoil leading-edge roughness. The roughness can be characterized by the roughness location, the roughness size, and the density of the roughness elements. (Studies have found roughness element shape of secondary importance.)

B. Iced-Airfoil Performance Parametric Studies

Several airfoil studies have been conducted to better understand the contribution of a geometric feature of an ice shape classification to the change in flowfield and the resulting aerodynamic penalties that result. These studies are reviewed more fully in Bragg et al.[3] and Broeren, et al.[18,2] Such studies contribute to a better understanding of the sensitivity of iced airfoil aerodynamics to the geometric parameters key for a given classification. This helps in the understanding of how to simulate ice with lower fidelity shapes and what is critical to be predicted by ice accretion computer codes. An example of horn ice sensitivity on airfoil aerodynamics is provided below.

Horn ice on airfoils usually results from glaze ice accretions. The dominant flow feature of airfoils with horn ice is a large separation bubble that exists as the flow separates from the ice horn. Failure of this flow to reattach leads to airfoil stall and large reductions in lift, increases in drag, and changes in pitching moment. The most important geometric features of horn ice are the height, location, and angle with respect to the flow over the upper surface horn. This determines much of the flowfield (dominated by the separation bubble aft of the horn) and the resulting airfoil aerodynamic performance. Figures 2 – 4, modified from Broeren et al.,[18] show the measured effect of simulated ice horn size and location on the lift, moment and drag of three typical subsonic airfoils.

Figure 2 summarizes the horn sensitivity study. In the study three different horn simple horn shapes were tested with three horn heights and three different horn tip geometries. These were tested at six different leading-edge locations with three on the upper surface, the leading-edge point, and two locations on the lower surface. In Fig. 2 one horn shape at three locations on the airfoil is shown. This matrix of horn heights, locations, and tip geometry was tested on three different airfoils: NACA 23012m, NACA 3415, and NLF 0414. The pressure distributions for these airfoils are shown all at $C_l = 0.5$, M=0.18 and Re = 1.8×10^6. Figures 3 and 4 show the effect of horn locations and heights, respectively, on lift, drag and pitching moment versus angle of attack. In Fig. 3 the change in airfoil performance with horn location is significant with the degradation in performance increasing as the horn moves from the lower surface around to the upper surface. In Fig. 4 horn height is increased from k/c = 0.02, 0.0433 to 0.0667, an increase of

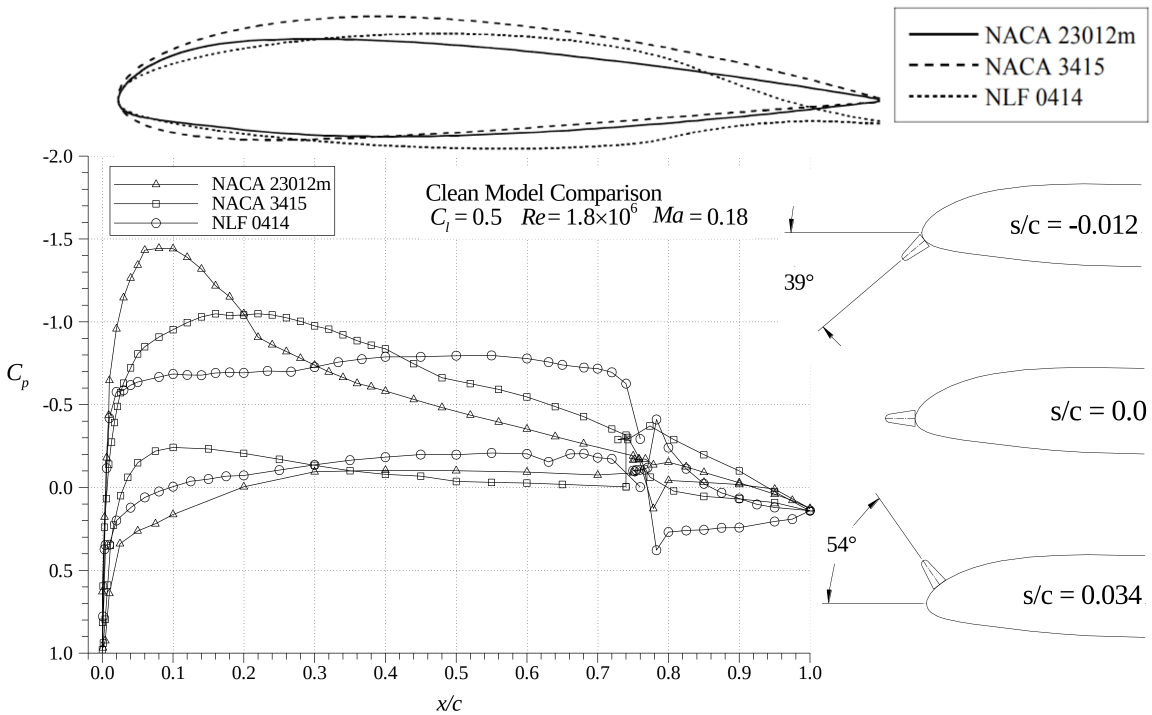

Fig. 2 Horn height and location simulations on three airfoils[18]

over 300 percent. The impact on the performance is significant with the large horn height causing the larger loss in performance, but the sensitivity is not as significant as to horn location as seen in Fig. 3. The relative impact of location and size for the horn on the NACA 23012m maximum lift is seen in Fig. 5. As expected from the earlier figures the impact of location is dominant over that of the horn height.

Airfoil geometry is also important as seen in Fig. 6. Here the NACA 23102m airfoil is seen to be much more sensitive to ice on the upper surface than the NLF 0414. Figure 2 shows the pressure distributions for these three airfoils at matched C_l. The 23012m was designed for high maximum lift and low pitching moment. To achieve this, it has very high surface velocity (low C_p) on the leading-edge upper surface and a large adverse pressure gradient downstream of the peak. The NLF 0414 airfoil is a laminar flow airfoil with an almost constant surface velocity, and therefore pressure, back to about 75% chord to maintain laminar flow. The impact of the higher surface velocity on the 23012m at the horn location and severe adverse pressure gradient at or just downstream of the horn causes larger aerodynamic losses due to the horn on the upper surface leading edge.

Based on these data and other data sets,[19,20] the sensitivity of classifications: ice horns, roughness and spanwise ridge shapes to location, size, etc. have been documented on several airfoil over a range of Re and M. From these data the required ice shape fidelity needed to achieve a given level of performance can be estimated and hence answer “how good is good enough” for many cases. Airfoil geometry is seen to be important as well and should be considered in the analysis.

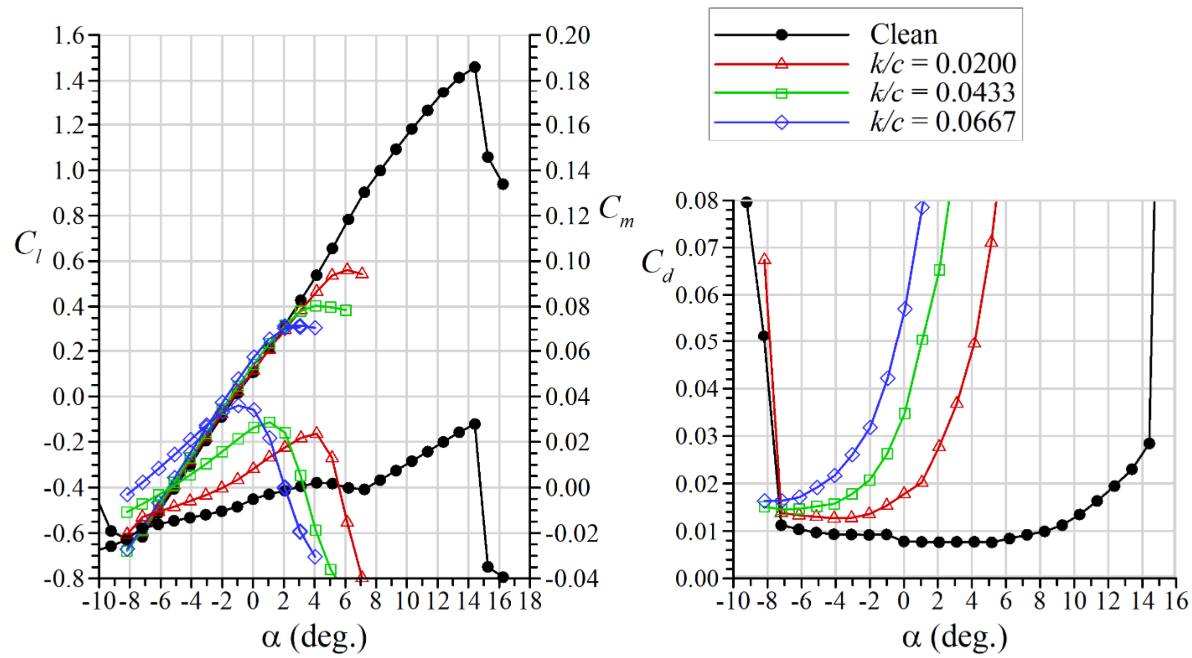

Fig. 3 Effect of horn location.[18] NACA 23012, Re=1.8x10^6, M=0.18

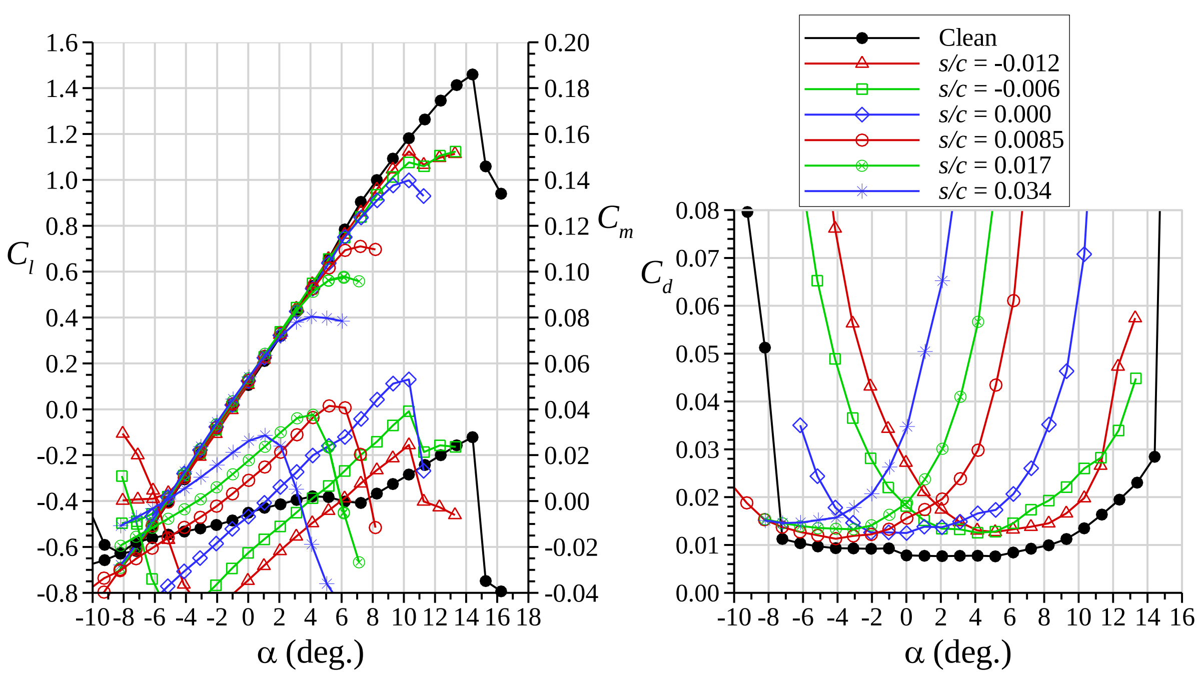

Fig. 4 Effect of horn height at s/c=0.034. NACA 23012, Re=1.8x10^6, M=0.18 (Ref [18])

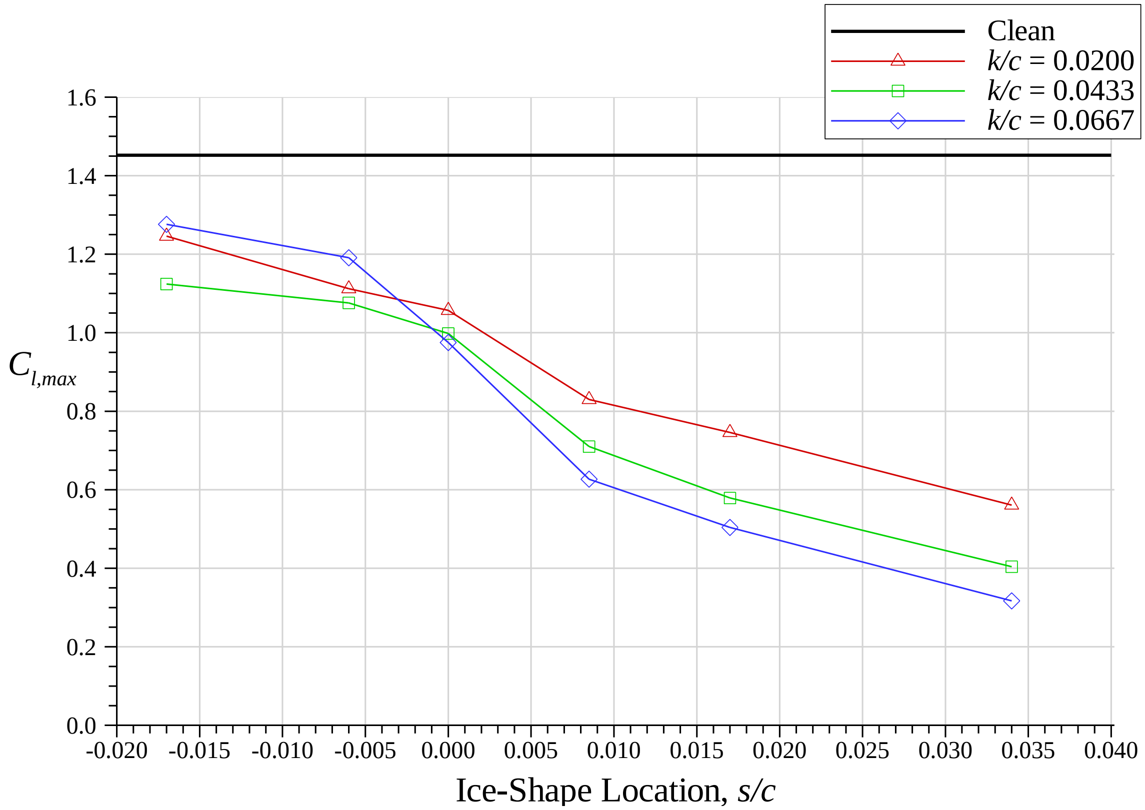

Fig. 5 Effect of horn size and location on maximum lift. NACA 23012m, Re=1.8x10^6, M=0.18 (adapted from Broeren et al.[18])

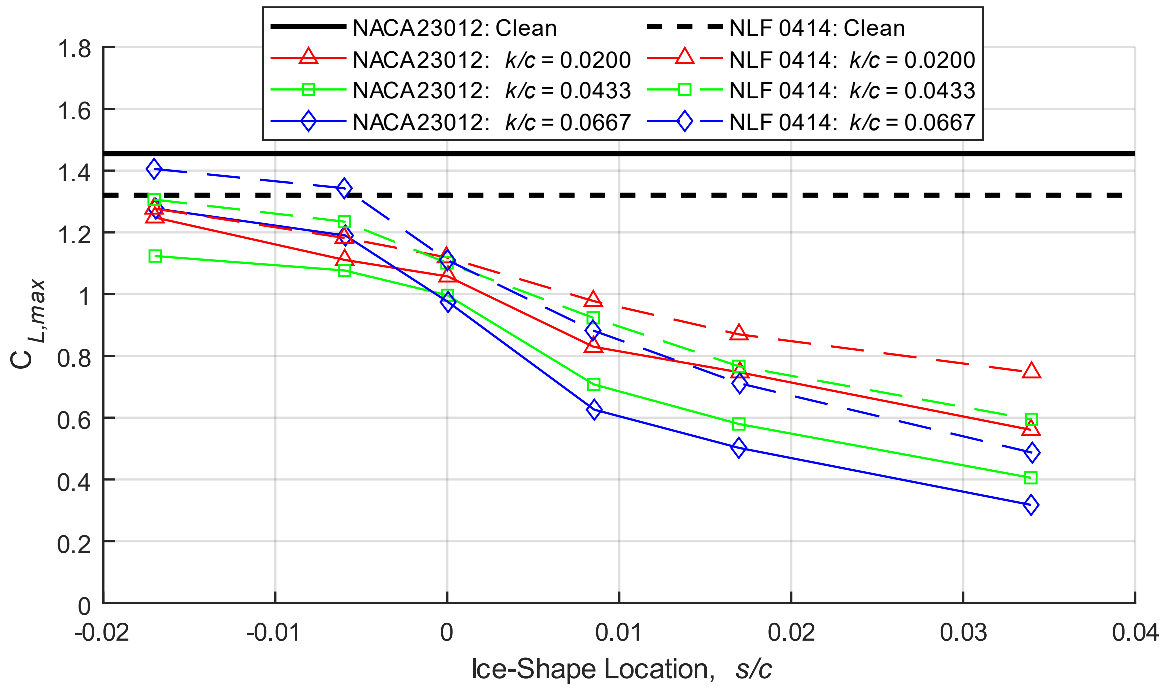

Fig. 6 Effect of horn location for two airfoil geometries. Re=1.8x10^6, M=0.18 (adapted from Broeren et al.[18])

III. Swept-Wing Ice Shape Classification

A. Background

The initial attempt to classify swept-wing ice shapes was presented by Broeren, et al.[2] in 2013. It relied heavily on the airfoil classification system[3] and the limited existing data on iced swept-wing aerodynamics and fundamental flow physics. Following the airfoil system, which was developed after extensive systematic and fundamental experimental studies, four classifications were proposed: roughness, streamwise ice, horn ice, and spanwise-ridge ice. The next few paragraphs follow the review and development from Broeren, et al.[2]

Fundamentals of the aerodynamics of swept wing are presented in the studies of Poll[21] and Furlong and McHugh[22] focusing especially on the leading-edge vortex that often forms as the angle of attack is increased. This leading-edge vortex results from leading-edge separation that reattaches downstream and, due to the spanwise pressure gradient, develops into a full or usually partial span vortex that is associated with the complex stall behavior of swept wings.

Some roughness studies on swept wings aerodynamics[23-25] are available from the literature. These classic studies show the effect of size and location but find little Re effect. A lack of flowfield information is available in the literature and more is needed including the parametric variation of size, location, and density.

Vargas[4] also found that streamwise ice generated by a rime accretion process showed no fundamental difference in geometry with different sweep angles. Only one study was found, Papdakis, et al.[26,27] where the ice shape increased the maximum lift coefficient. This has been seen in the airfoil case[28] as well and affects the flow similar to a leading-edge device. This is not, however, the usual case for airfoils and is assumed to be a special case for swept wings as well. Data from more streamwise ice geometries are needed and especially experiments that also provide flowfield data.

Papdakis, et al.[29] studied spanwise-ridge ice on a swept-wing geometry for a range of simple ice shapes at low Re. For most cases a decrease in lift-curve slope and increase in drag were measured. However, the maximum lift and stall angle increased. This also appears to perhaps be a special case which was also seen in the airfoil case. Whalen[30] and Papadakis et al.[31] both observed that when the clean airfoil exhibited trailing-edge stall and the height of the spanwise ridge ice simulation was comparable to the local boundary-layer thickness, the iced airfoil performed better at angles of attack near and above clean wing stall. This performance enhancement was attributed to the mixing layer generated by the ice shape entraining higher-momentum fluid into the boundary layer. Broeren et al.[32] showed that this lift enhancing effect on airfoils can be an artifact of low-Reynolds number testing of the clean airfoil. As in the streamwise ice case, more data are needed to further explore this, especially at higher Re and with flowfield measurements.

Horn ice shapes on swept wings have received more attention than either streamwise or spanwise-step ice accretions. This classification of shapes has also been more heavily studied in the airfoil icing literature as well.[3] For swept wings Vargas[4] found a significant effect of sweep angle on the glaze ice geometry. Depending upon the sweep angle, air temperature, cloud liquid water content, and other factors, highly three-dimensional features called "scallops" or "lobster tails" may form. No airfoil equivalent exists to this swept-wing icing phenomena. Vargas[4] identified sweep angle and icing conditions leading to: no scallops, incomplete scallops, and complete scallop glaze and mixed ice accretion. The complete scallops are distinguished by regular gaps in the spanwise direction in the glaze ice horns. The reader is referred to Vargas[4] for much more information on scallop ice formation.

For the aerodynamics of swept-wing horn ice Broeren et al.[2] relied on two different sets of experimental data. Bragg et al.,[33] Kwon and Sankar,[34] and Khodadoust and Bragg[35] performed a more fundamental flowfield and wing aerodynamics study on a simple geometry horn ice shape on a low aspect ratio swept wing at low Reynolds number. Papdakis et al.[36-38] examined the performance of measured and LEWICE predicted ice shapes on a swept wing at low Reynolds number.

Bragg et al.[33] performed a flowfield study on a swept wing using Laser Doppler Velocimetry (LDV) to measure all three components of velocity behind a simulated glaze ice shape. Their experimental results were complemented by the computational results of Kwon and Sankar.[34] The model tested was a rectangular semispan wing with a NACA 0012 section, a chord of 15-in., sweep angle of 30 deg., and an aspect ratio of approximately 2.3. The ice shape was produced by uniformly extending a horn ice shape formed on a NACA 0012 airfoil in NASA's Icing Research Tunnel. A cross-section of the ice shape is shown in Fig. 7. The ice shape generated a leading-edge vortex that can clearly be seen in the constant pressures on the upper surface leading edge on the right plot in Fig. 8. The Kwon and Sankar computational results compared well to the surface pressure and LDV measurements for this swept wing with ice. Figure 9 shows the computational surface oil flow and CFD particle trajectories that clearly show the ice-induced leading-edge vortex. The 3D LDV measurements reported by Bragg et al. also show the leading-edge vortex and its reattachment, the extensive spanwise flow and separation, and the development of the flow both spanwise and streamwise.

The Papadakis study[36-38] looked at a swept wing with complete scallops (the most three dimensional), incomplete scallops, and the least three-dimensional shapes based on LEWICE calculations. The scallop shapes came from IRT tests. The most interesting results for our purposes here are those comparing a complete scallop test from an IRT high-resolution casting and the much less 3-D LEWICE shapes. Figure 10 shows the Cp for Ice6 (IRT-IPSF22) highly three-dimensional ice accretion geometry typical of complete scallops. In this case, both the smooth and rough LEWICE shapes (LS-IPSF22 and LR-IPSF22) exhibited a clearly identifiable region of approximately constant pressure from $x/c \approx 0.06$ to $x/c \approx 0.2$ associated with the leading-edge vortex. In contrast, the pressure distribution for the Ice6 (IRT-IPSF22) shows a very different leading-edge pressure distribution. Here the nominally two-dimensional LEWICE shapes show a distinct region of approximately constant pressure that has been shown to correspond to the leading-edge vortex. For the highly three-dimensional geometry of the complete scallop ice casting simulations, this pressure region was not observed. Broeren et al.[2] suggest that the need for an aerodynamic subclassification of horn ice that distinguishes between "nominally three-dimensional" horn ice and "highly three- dimensional" horn ice. Nominally three-dimensional horn ice is associated with glaze ice accretion having either no scallops or incomplete scallops where the gross shape does not vary significantly over small spanwise distances. Highly three-dimensional horn ice is associated with glaze ice accretion having complete scallop tips and rapidly changing geometry spanwise. This suggestion is developed later in the paper based on more recent results.

While these two experimental studies provide some flowfield information and some highly 3D scallop iced swept wing data, a significant need for data still exists. The ice shapes tested were not accurate representations of actual full-scale ice shapes of interest and no high Reynolds number data were available. These issues were addressed in the Swept-wing icing program conducted by the authors and their colleagues[1] and are discussed in the next section.

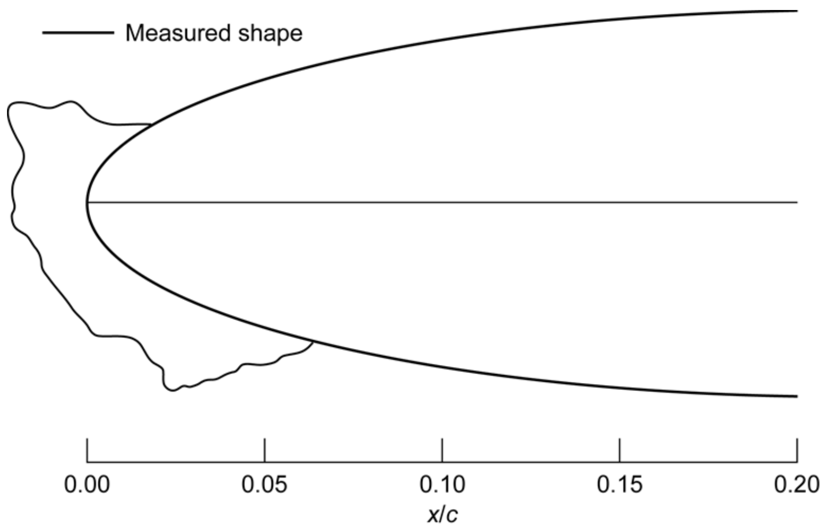

Figure 7. NACA 0012 swept horn-ice-shape cross section, after Bragg et al.[33]

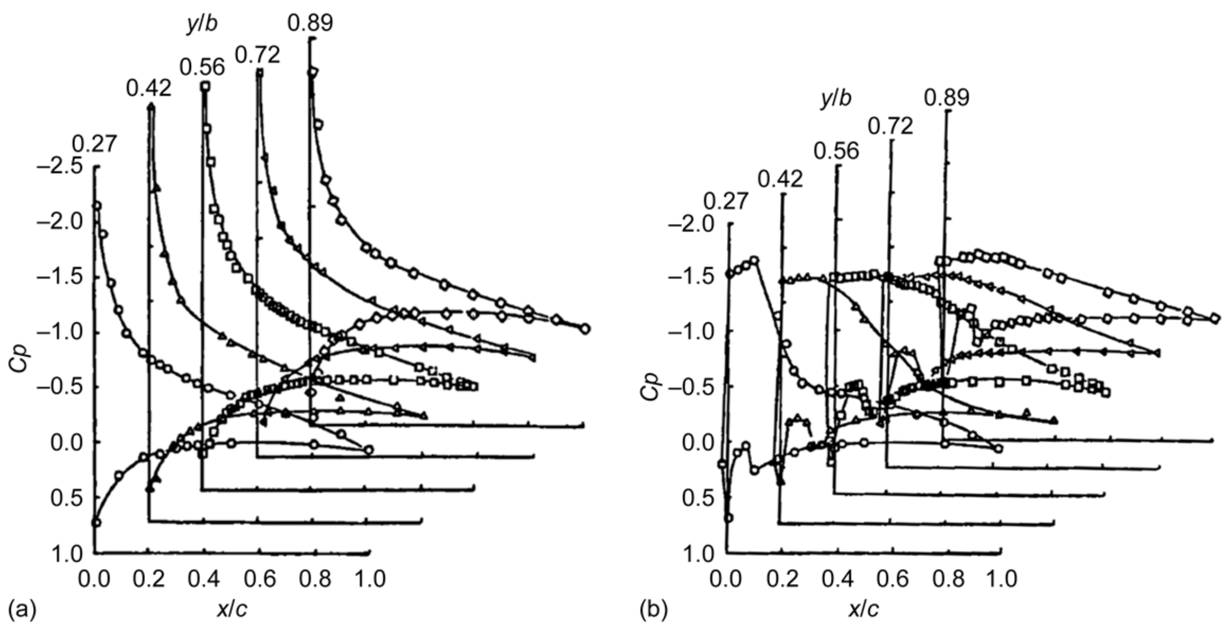

Fig. 8 Pressure distributions for the NACA 0012 swept wing with and without the horn ice shape, α = 8°, Re = 1.5x10^6, after Khodadoust and Bragg.[33] (a) Clean wing. (b) Wing with glaze ice.

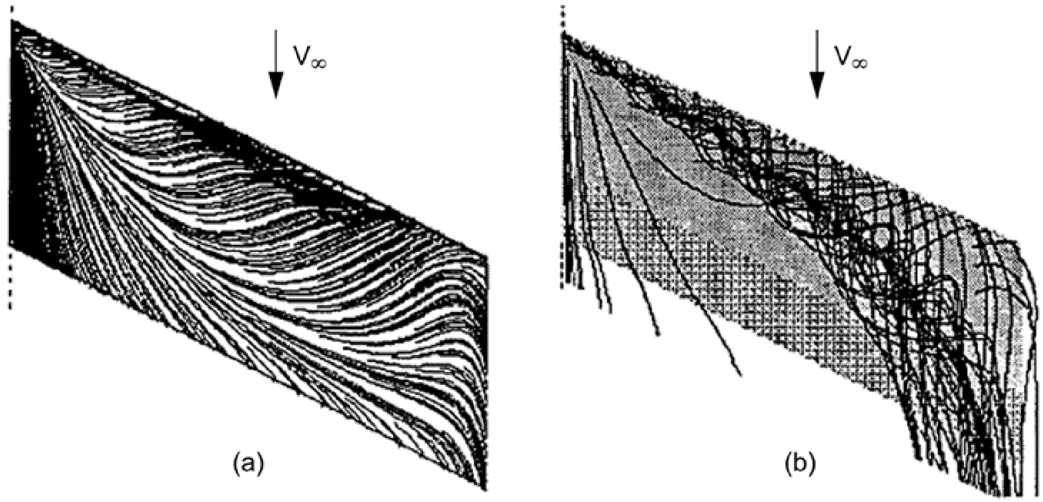

Fig. 9 Flowfield over the NACA 0012 swept wing with horn ice shape. (a) CFD surface oil simulation. (b) CFD particle trajectory simulation, α = 8°, Re = 1.5x10^6, after Kwon and Sankar.[34]

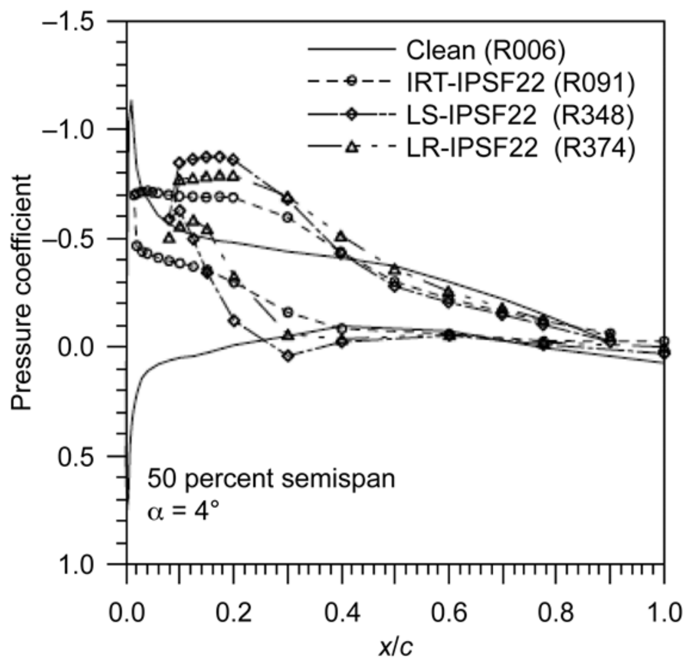

Fig. 10 Effect of IRT Ice6 (IRT-IPSF22) and LEWICE ice-shape simulations on GLC-305 swept wing at Re = 1.8x10^6, after Papadakis et al.[36]

B. Current Iced swept aerodynamics results

Based on the aerodynamic and flowfield data acquired since 2013 in the swept-wing icing research program additional information is now available to update the swept-wing ice shape classifications of Broeren et al.[2] In this program, the majority of the aerodynamic testing was on horn shapes as represented by varying fidelities of horn ice accretions including scalloped shapes. Only one of the accretions tested was a streamwise ice shape and no spanwise ridge or leading-edge roughness cases were accreted in the icing tunnel or tested in a dry-air tunnel for its aerodynamics. The ice shape names and accretion conditions are shown in Table 1.

Table 1. Icing conditions for the six ice accretion cases.

RunID—Name	AoA (deg.)	Speed (kt)	T_{total} (deg. C)	MVD (μm)	LWC (g/m³)	Time (min)
3—Venetian Blind	3.7	130	-3.8	25	1.0	29
4—Maximum Scallop	3.7	130	-6.3	25	1.0	29
5—Small Gap	3.7	130	-8.7	25	1.0	29
6—Incomplete Scallop	3.7	130	-11.2	25	1.0	29
9—Streamwise/Rime	3.7	130	-17.9	25	0.6	23
23—WB33 Direct App. C	3.7	130	-3.1	25	0.9	45

Horn ice shape results:

Thus, referring to Fig. 1 on the airfoil classification process, and the swept wing ice classification already put forward by Broeren et al.,[2] the contribution of the current swept-wing icing study is to better understand the horn ice classification. In the analysis of Broeren et al.[2] the authors noted the difference in the pressure distributions on an IRT measured complete scallop ice shape simulation on a swept wing and a LEWICE prediction and simulation that did not have the spanwise variation and regular gaps as seen in a scalloped shape, Fig. 10. These differences were referred to as highly 3D (complete scallops) and nominally 3D horn shapes. The current research benefits from having also tested low-fidelity simulations of the complete scalloped shapes to provide a better understanding of the effect of the highly 3D geometry. These measured scallop shapes were carefully generated and are thought to be accurate representations of full-scale ice accretions on a swept CRM65 wing in actual full-scale icing conditions. The current study also has extensive pressures measurement on the swept wing and surface flow visualization to provide some understanding of the flowfield. Key results from this research are presented below.

In this research program the majority of the testing was on horn shapes as represented by various degrees and fidelities of scallop ice accretions.[12-17] Based on these data, there appear to be two key flowfield features that result from highly 3D and nominally 3D horn ice shape geometry. The two flowfield features result from differences in the formation and development of the leading-edge vortex that dominates these flowfields at moderate to high angle of attack. At this time these two flowfield types are referred to as Type I and Type II. More recent analyses of type I and II flows are given in by Broeren et al.[39] and Lee et al.[40]

Type I flowfields are dominated by spanwise-running leading-edge vortices generated by flow separation from the leading-edge ice accretion. Similar flowfields are well known and generated from leading-edge separation that can occur on clean, swept wings as documented by Poll[21] and others. This is roughly the 3D extension of the separation bubble widely studied in the horn ice airfoil case. It may be one single vortex from root to tip, or more often multiple leading-edge vortices as a result of the spanwise-varying leading-edge ice-accretion geometry and its interaction with the highly 3D swept-wing flowfield. The type I flowfield was common for low-fidelity ice shapes which did not have highly 3D features, such as scallops. The type II flowfield lacks the leading-edge spanwise vortex seen for the more uniform spanwise 3D horns. In the oil flow visualization this flowfield is observed to exhibit multiple streamwise-running streaks of oil appearing to emanate from the spanwise gaps in the scallop geometry. These features appear to dominate the flowfield through the useable lift coefficient[14] and angle of attack range, suppressing the leading-edge vortices for all or significant portions spanwise of the wing.

More likely, these streaks are the result of counter-rotating vortices emanating from the scallop features and repeating as the scallops repeat spanwise on these shapes. Figure 11 from Diebold[41] shows an oil flow visualization on the upper surface behind a large scallop ice shape which repeats (as indicated by the red lines) spanwise. This is a small-scale experiment at low Reynolds number (3×10^5) on a CRM semispan model at AoA = 3 degrees. The section of the wing shown is from just outboard of the Yehudi break to 75% span at the tip of the photo. Each section of the flow, bordered by the red lines, shows an almost identical flowfield containing three “cells”, Fig. 12.

Each cell is generated by a pair of counter rotating vortices which attach to the surface in the center of the cell and lift off where the red dashed lines show the oil flowing together and pooling. This flow pattern is very clear in these photos due in part to the flow visualization method used, but also likely due to the large scallops and low Reynolds number.

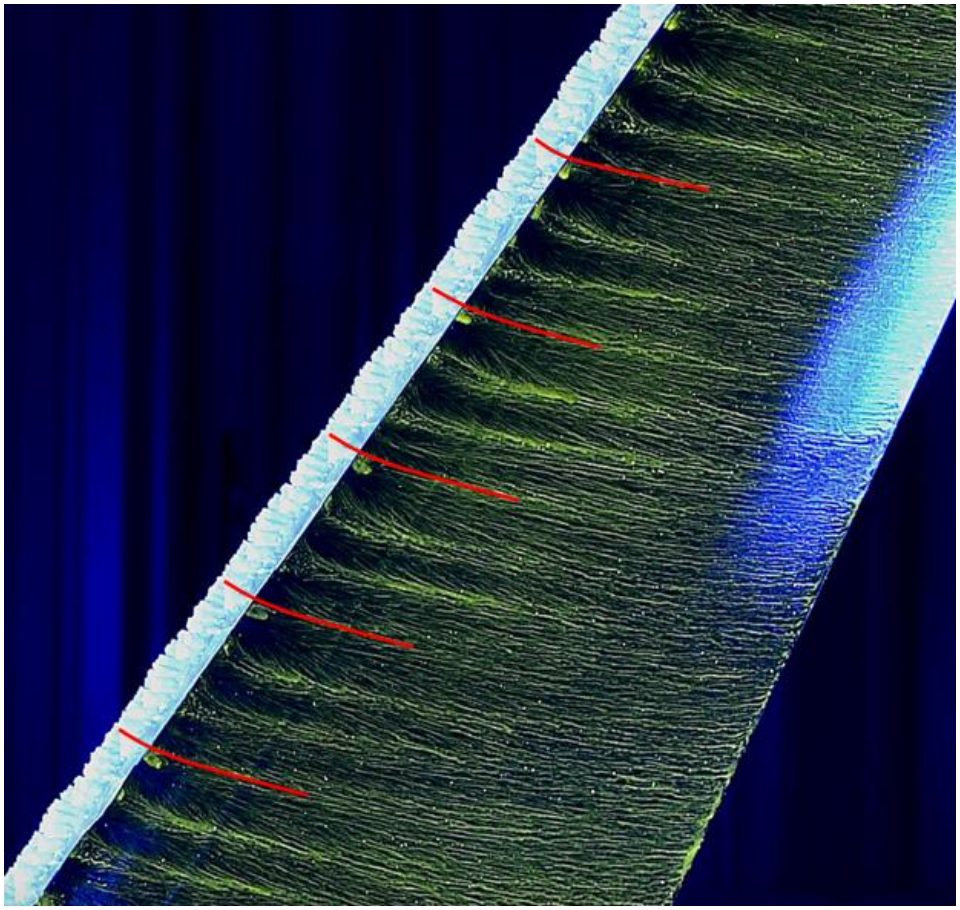

Fig. 11 Oil flow visualization behind a high-fidelity scallop shape on a swept wing at Re = 3x10^5 and AoA = 3 deg. CRM wing. Red lines indicate where ice shape repeats.[41]

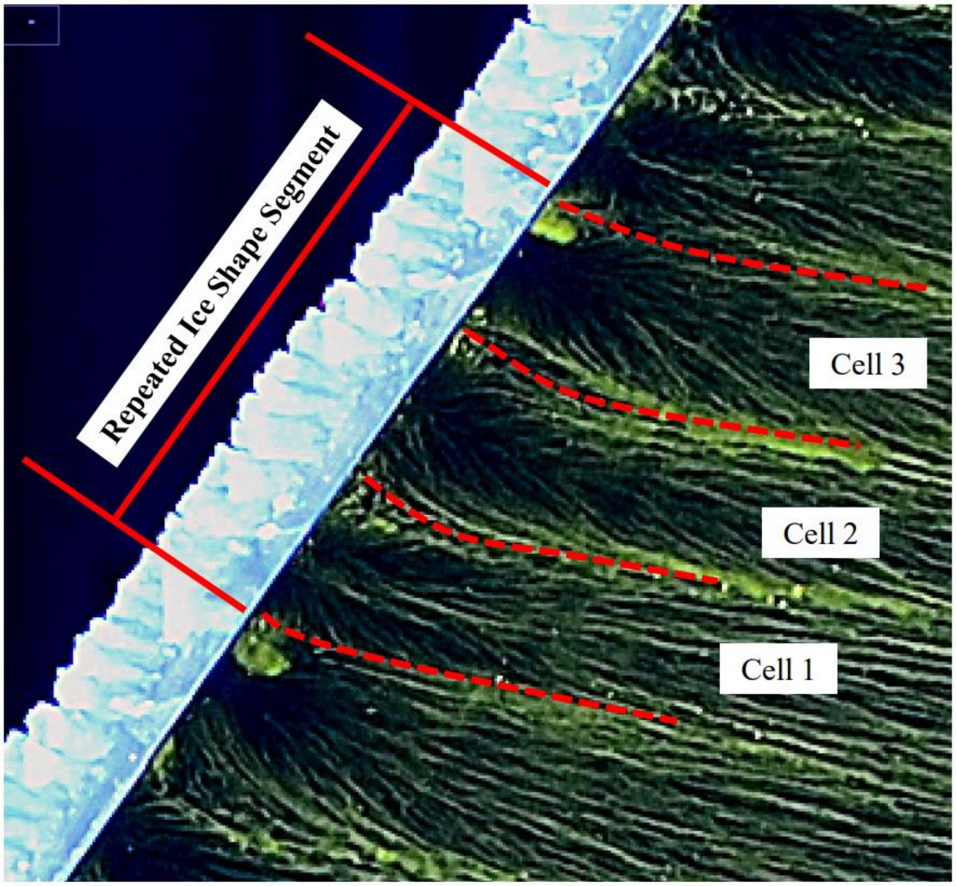

Fig. 12 Close up of oil flow visualization behind a high-fidelity scallop shape on a swept wing at Re = $3x10^5$, AoA = 3 deg.[41]

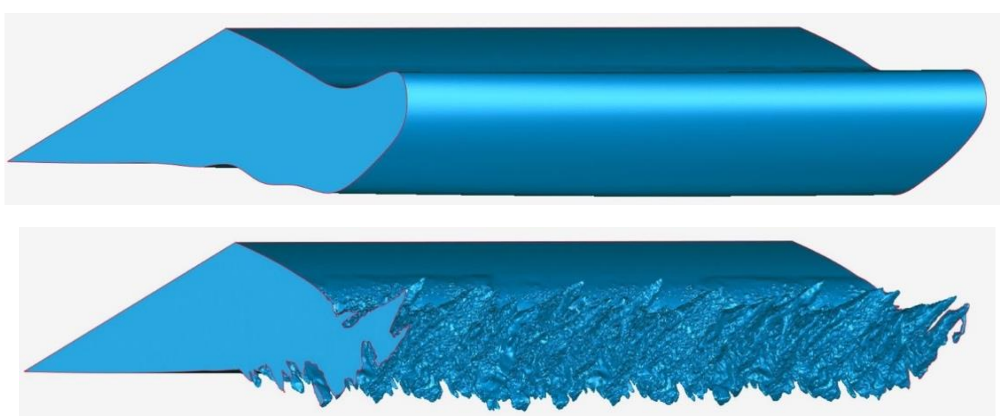

Fig. 13 3D smooth max and high fidelity scallop ice shapes[17]

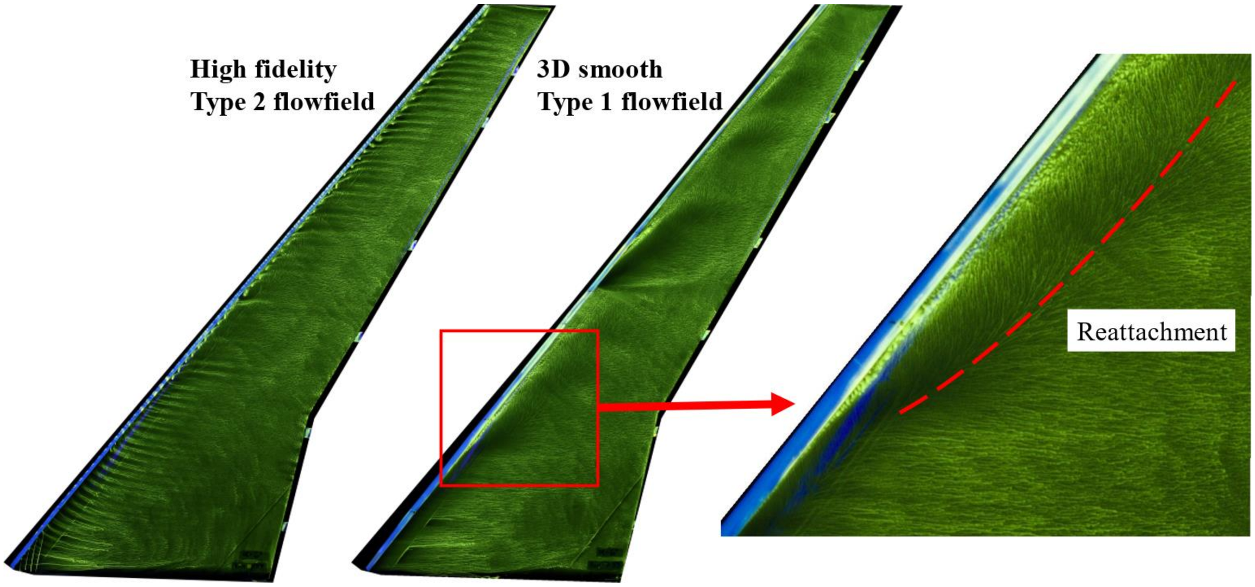

Fig. 14 Max scallop high fidelity and 3D smooth oil flow at α = 6.4 deg.

The type I and type II flowfields and the corresponding ice shape geometries can be better understood by considering the high-fidelity maximum scallop ice shape and the lower fidelity version referred to as the 3D smooth maximum scallop ice shape. These are depicted from their CAD representations in Fig. 13.

Figures 14 and 15 show surface oil flow and streamwise pressure distributions at 6 spanwise stations, respectively, for the 8.9% scale CRM65 wing with the 3D smooth and high-fidelity maximum scallop ice shapes at an AoA of 6.4 degrees.[17] In Fig. 14 the high-fidelity shape clearly shows the type II flowfield. This is seen as the series of streamwise streaks in the oil originating from the leading-edge ice simulation and extending streamwise to the midchord and beyond. At this angle of attack the oil streaks are seen from root to tip, and no evidence of organized spanwise vortices is seen. No evidence of a leading-edge vortex is present in the surface oil. However, the 3D smooth surface oil flow is very different. First, there are no streamwise streaks in the oil. Instead, careful examination reveals leading-edge separation at various locations across the span. One of these vortices is highlighted in Fig. 14 where the vortex reattachment is shown.

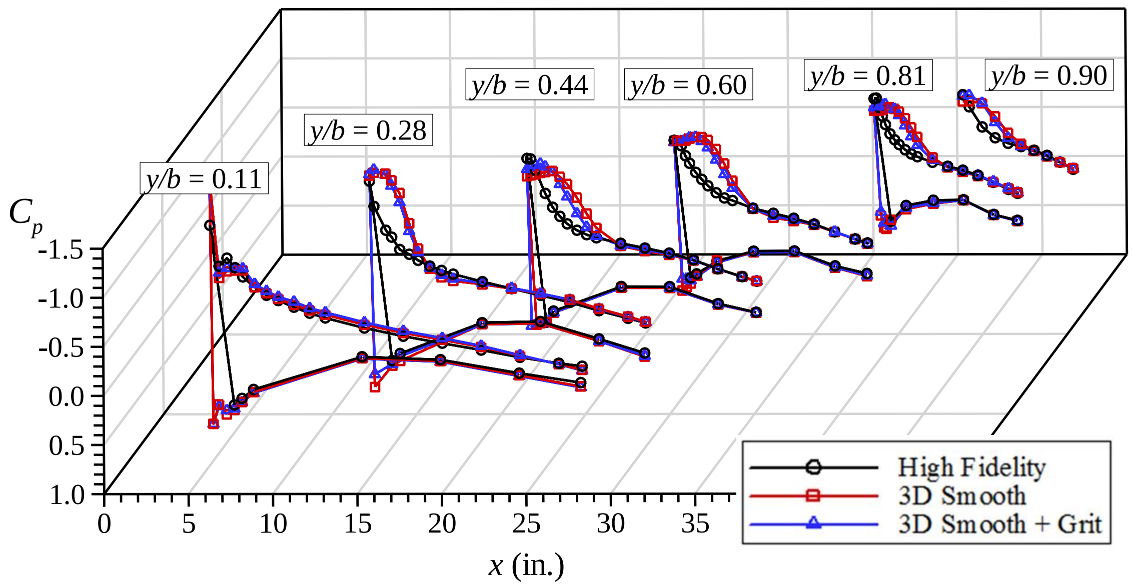

Fig. 15 Surface Pressures for Maximum Scallop Configurations at α = 6.4 deg.

Figure 15 displays the surface pressure coefficients on the 6 chordwise rows across the model. Pressures are shown for both the high-fidelity and the 3D smooth ice shapes as seen in Fig. 13 in addition to the pressure for the 3D smooth with grit (surface roughness). The pressure for the 3D smooth and 3D smooth + grit is very similar indicating little effect of the grit. The leading-edge vortex can be seen in the surface pressures as the small region of almost constant pressure on the leading-edge, upper surface of the model. This is the pressure on the model surface under the leading-edge vortex. For example, on the second spanwise row under the label y/b=0.28 the 3D smooth and 3D smooth + grit pressure coefficients are relatively constant for about two inches and then quickly return to pressures that match the high-fidelity case about 20 percent chord downstream as the external flow returns to the airfoil surface. This constant pressure plateau is seen for every pressure distribution moving outboard to the final tap row at y/b=0.90. This indicates the presence of a spanwise leading-edge vortex aft of the ice shape at these tap locations. For each spanwise row the high-fidelity shape C_p's show a suction peak at the leading edge and no constant pressure, separated flow, region.

Figures 16 and 17 show the surface oil flow and surface pressure, respectively, for these same ice shapes at a higher angle of attack at 8.4 degrees. The high-fidelity shape again shows the streamwise running streaks near the root, but they appear less well defined passed the Yehudi break moving outward spanwise. Looking carefully, periodic pooling of the oil is seen aft of the ice shape beyond the Yehudi break indicating the presence of the oil streaks and local separation

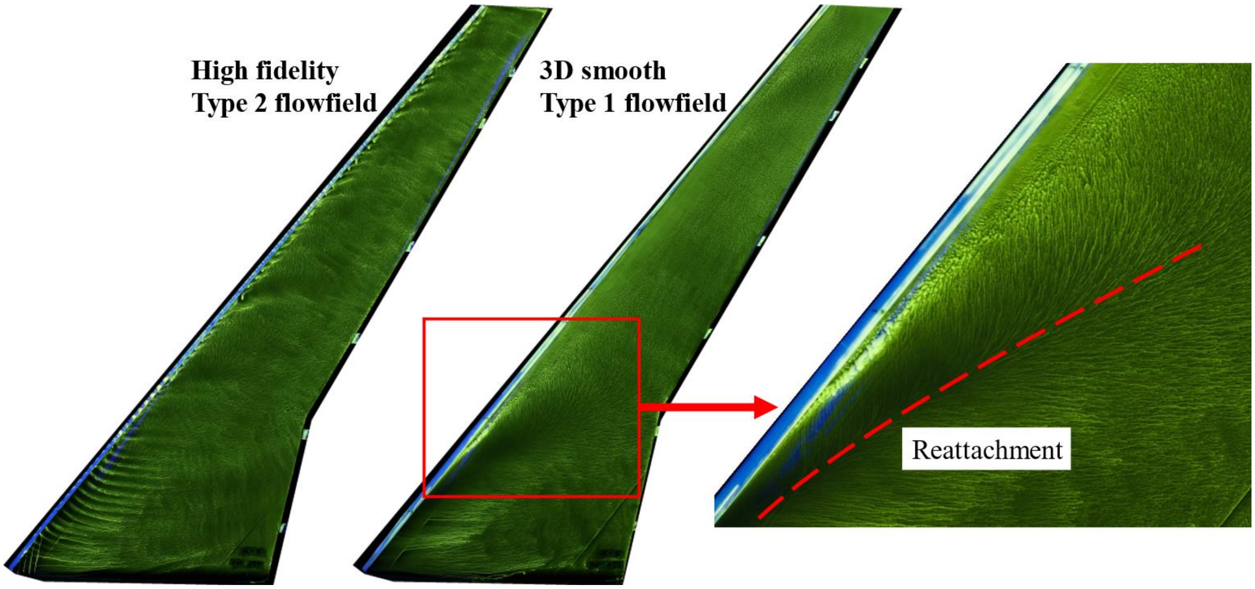

Fig. 16 Max scallop high fidelity and 3D smooth oil flow at α = 8.4 deg.

regions, but no organized spanwise vortices. The 3D smooth oil flow shows a spanwise-running, leading-edge vortex near the root that appears to grow significantly in chordwise extent as it moves spanwise. Significant separation is seen further outboard as the very low shear results in little movement of the oil. In the surface pressures of Fig. 17 for the 3D smooth shape, note the extensive constant pressure plateaus at y/b = 0.44 and 0.60 indicating very large regions of separated flow. Remember that the end of the pressure plateau does not necessarily indicate attached flow which instead usually occurs well aft of this chordwise location as pressure recovery takes place as the vortex reattaches. At this angle of attack the high-fidelity ice shape configuration at y/b=0.44 and 0.60 shows what is probably some leading-edge flow separation as the sharp pressure spike seen inboard, and at the lower angle of attack, is no longer present and instead the Cp broadens chordwise. Thus, inboard where the oil flow still shows distinct streamwise oil streaks and no leading-edge vortex, a sharp pressure spike is present for the high-fidelity case.

Figure 18 shows the aerodynamic performance of the high-fidelity max scallop shape and the low fidelity simulation, 3D smooth, with and without grit roughness.[17] The 3D smooth shape is seen to be nonconservative in over predicting the maximum lift and underpredicting the drag. The addition of the grit improves the simulation, but the results are still nonconservative.

.

.

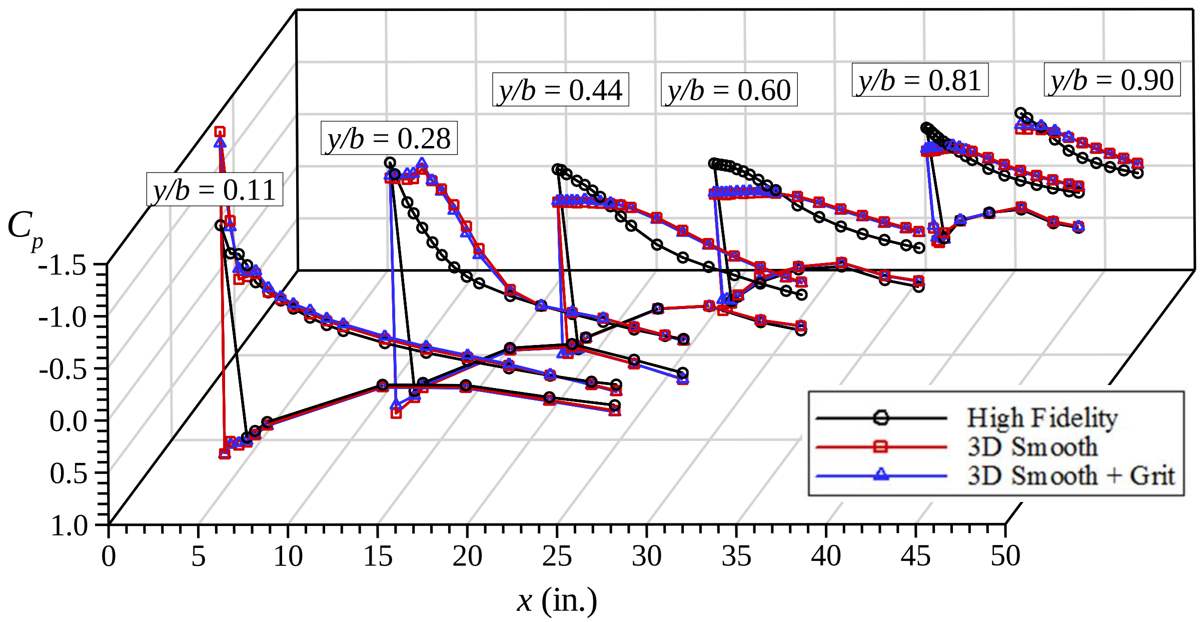

Fig. 17 Surface Pressures for Maximum Scallop Configurations at α = 8.4 deg.

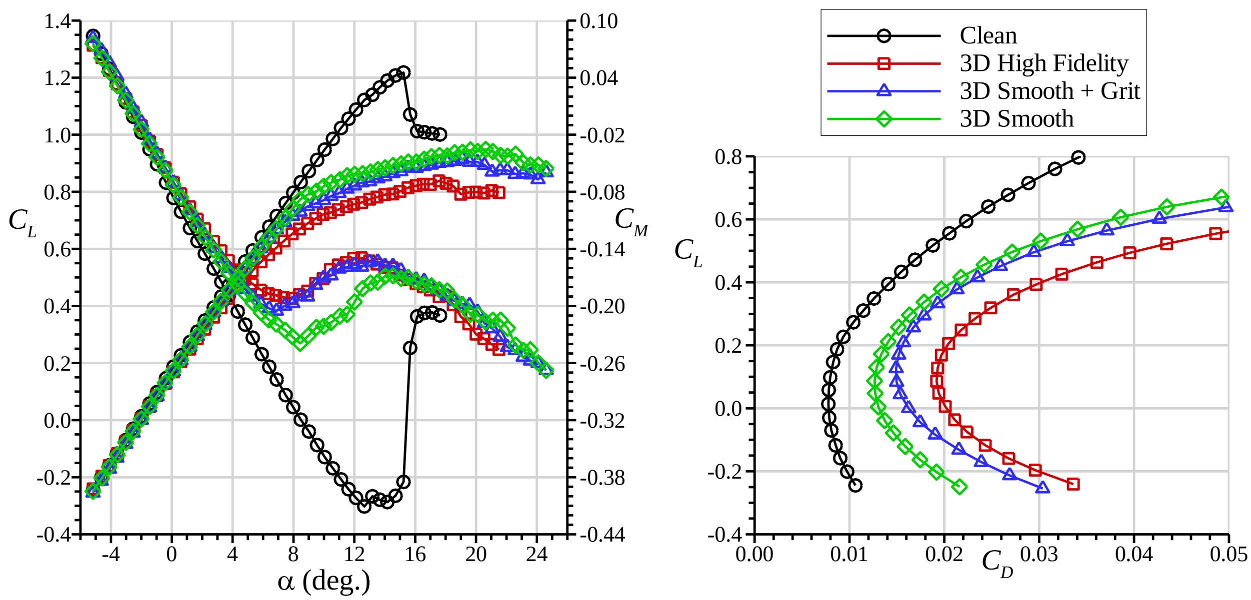

Fig. 18 Aerodynamic performance comparison between the four fidelity representations of the Maximum Scallop ice shape at Re = 11.9×10^6, M = 0.23. (Woodard, et al. [17])

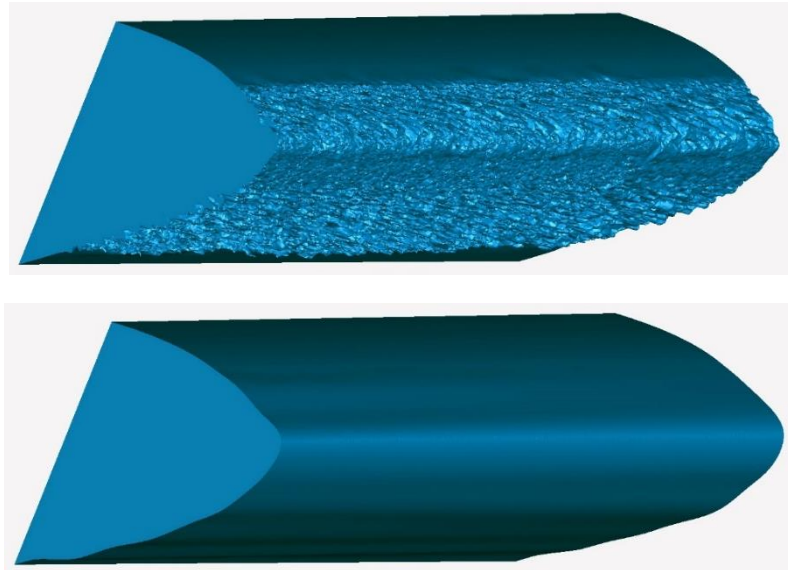

Fig. 19 Streamwise high fidelity (top) and 3D smooth (bottom) ice shapes

Streamwise ice shape results:

The streamwise ice shape was generated in rime icing conditions in the NASA IRT as shown in Table 1. As with the other accretions in Table 1, an aerodynamic wind tunnel test was conducted for the CRM65 swept wing with the full-span high-fidelity ice shape as well as a lower fidelity 3D smooth shape. Camello et al.[12] presented the first and most detailed discussion of the effect of fidelity on the streamwise ice shape aerodynamics. Figure 19 shows a segment of the high-fidelity ice shape as well as the 3D smooth low-fidelity shape. The 3D smooth version lacks the irregular features at the leading edge that are present in the high-fidelity shape. This will be seen to significantly affect the aerodynamics.

The lift, moment, and drag for the high-fidelity, 3D smooth, and 3D smooth with roughness are shown in Fig. 20. Note that the high-fidelity and 3D smooth data were only taken at angles of attack up to 16 degrees. The lift for the three ice shape simulations looks very similar up through maximum lift, although the 3D smooth with grit has a slightly lower maximum lift. The high fidelity and 3D smooth plus grit have similar drag performance over the angle of attack range with the 3D smooth showing lower drag. The pitching moment comparison follows from the lift. Here the 3D smooth plus grit results compare well with the high-fidelity up to 12 degrees angle of attack. This agrees well to the lift performance where these two ice shapes also diverge at about 12 degrees AoA. The 3D smooth pitching moment for angle of attack greater than two degrees has a more negative, nose-down pitching moment. Both of the 3D smooth pitching moment curves show a

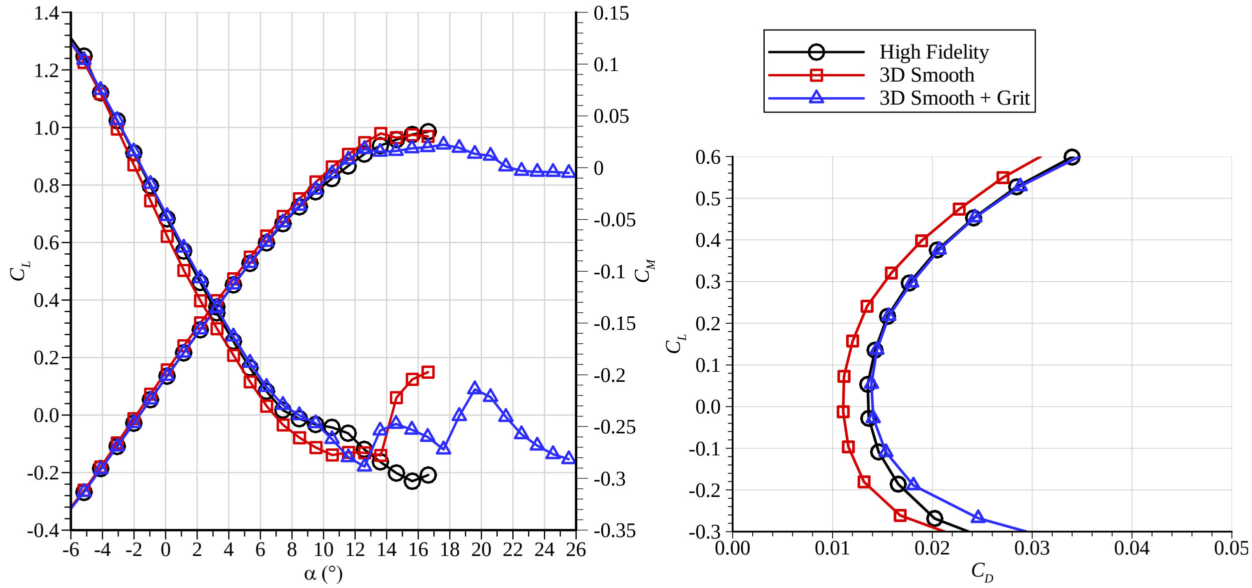

Fig. 20 Streamwise ice aerodynamic performance. Re = 1.6 x 10^6 and M = 0.17

nose-up break at around 12 degrees angle of attack defining the range of useable lift. The high-fidelity shape breaks later but more data at higher angles of attack are needed to define the angle.

Upper surface oil-flow visualization is shown in Fig. 21 for the high-fidelity streamwise ice shape and the 3D smooth shape at 9.5 degrees angle of attack. In the high-fidelity ice shape visualization we can see massive flow separation at, and just outboard of the Yehudi break. Further out spanwise and almost to the wing tip, streamwise oil streaks can be seen similar to those discussed earlier in the section on Horn Ice Results. In the horn ice case these streaks were produced by the flow through and around the highly 3D horn ice scallops and were believed to be the result of streamwise vorticity generated by the geometry. Here for this streamwise ice shape, it appears a similar phenomenon is occurring with streamwise vorticity generated by the very nonuniform leading-edge geometry of the high-fidelity streamwise ice shape. Just as in the horn case, this streamwise vorticity is affecting the flow in this region. This phenomenon does not seem as consistent across the span as in the horn case. Perhaps this is due to the variation of the ice shape across the span and the fact that the streamwise vorticity generated may not be as strong as in the horn case. Further measurements are needed to more fully understand this flowfield.

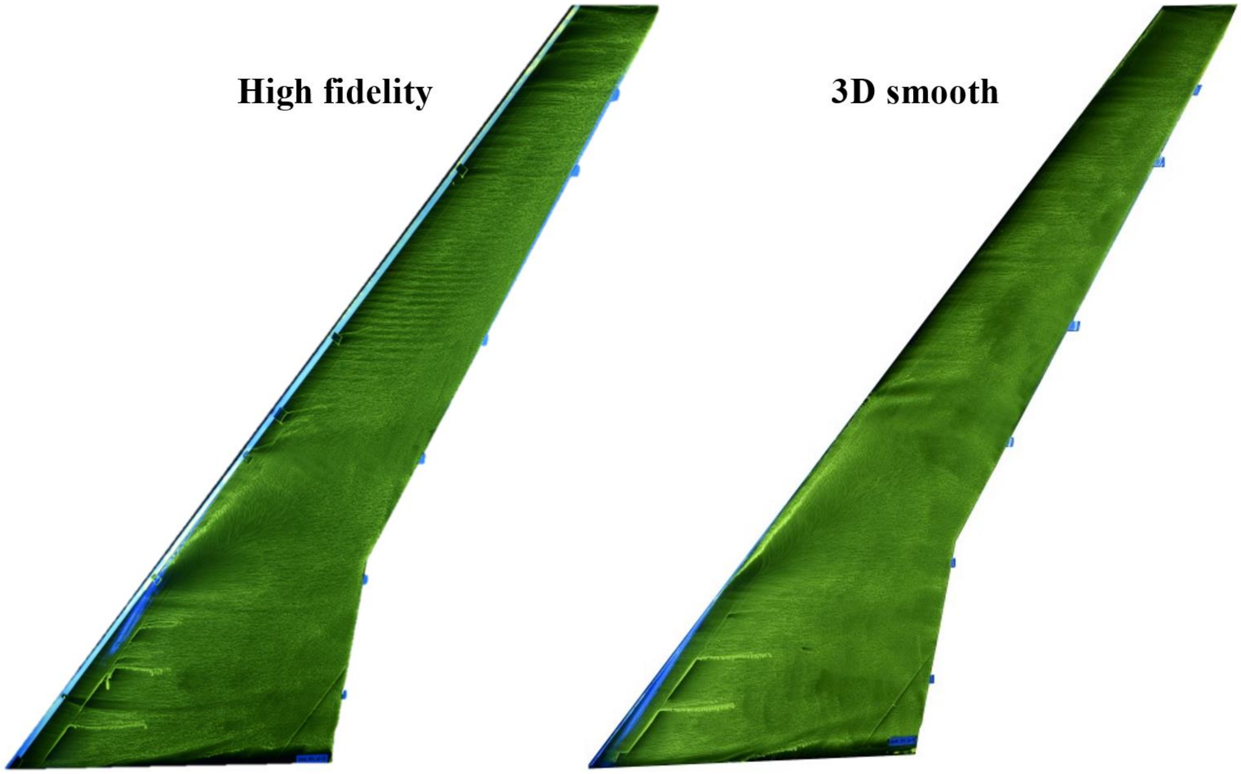

Fig. 21 Streamwise high fidelity and 3D smooth oil-flow visualization at Re = 1.6 x 10^6 and M = 0.18, α = 9.5°

Figure 22 shows the surface pressure coefficients measured at the six streamwise tap rows for the three ice shape configurations at an angle of attack of 9.5 degrees. Here the black circles are the high-fidelity ice shape and it shows a large separation (nearly constant Cp from the leading edge to about 20 percent back on the chord) at y/b = 0.44. A smaller almost constant pressure region is also seen at y/b = 0.28 and is due to the increased pressure under the leading-edge separation vortex. This corresponds to the separation seen around the Yehudi break spanwise location in the flow visualization. Outboard of this station at y/b = 0.60, 0.81, and 0.90 a very peaky leading-edge pressure distribution is seen with no constant pressure region. As discussed in the Horn Section this represents the low pressure on the leading-edge as the vortex is suppressed by the ice shape geometry and the flow remains attached on the leading edge. This is the region where the oil streaks are seen on the outboard leading-edge section in Fig. 21.

The 3D smooth with grit has similar pressure to the high-fidelity while the 3D smooth sees slightly more suction on the leading edge. Note for example the y/b = 0.28 station. Here very clearly the 3D smooth has the peaky, no leading-edge vortex distribution, and the 3D smooth with

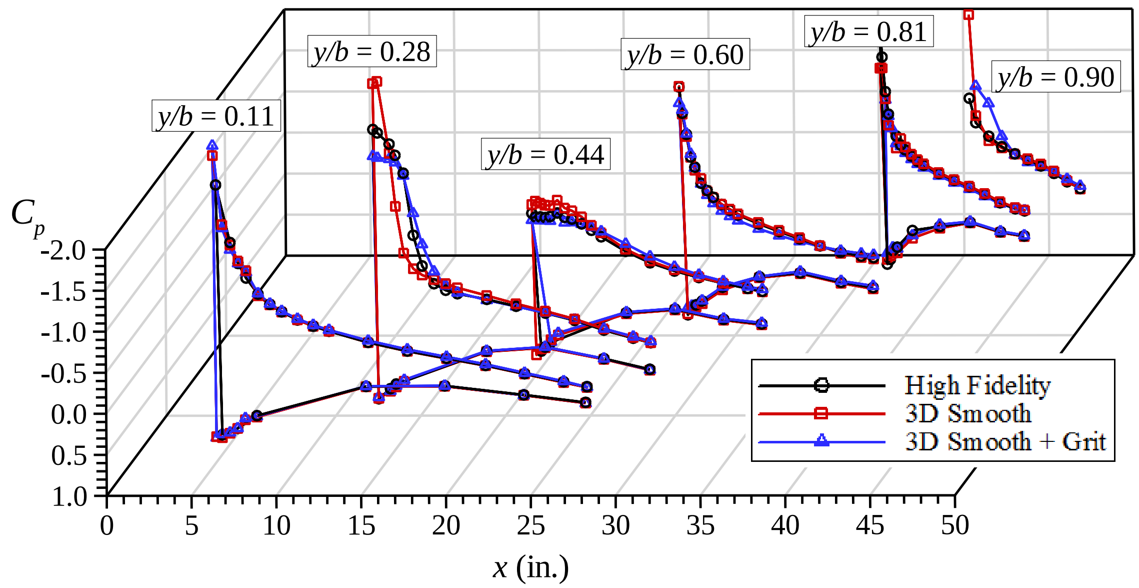

Fig. 22 Streamwise ice surface pressures at α =9.5 deg. Re = 1.6x10^6 and M = 0.18

grit has the C_p of the leading-edge separation case. Consistently, the 3D smooth plus grit and the high-fidelity have very similar flowfields as represented by the measured surface pressure distributions in the region of the Yehudi break where the leading edge separation first appears.

Thus, for the streamwise ice shapes the type I and type II flowfields discussed in the Horn Section are also seen here. However, in some ways this flowfield on the streamwise shape seems more complex. Perhaps this is because the streamwise geometry is not as highly 3D as the scallop shape discussed in the horn section and that here the type I and II flowfields vary across the span. It is also interesting that adding the surface roughness is seen to best generate the pressure field seen in the high-fidelity case. There is not enough flowfield information to discern if this is by the same flow mechanism, but it does suggest a highly complex flowfield that must be better understood before the key geometric parameters can be identified with confidence and the goal of accurately simulating its aerodynamic effect with simple geometric shapes achieved for the general streamwise ice classification.

C. New Swept-wing classification

Using the 2013 swept wing ice shape Classification of Broeren et al.[2] the scalloped ice shapes tested of any fidelity would be classified as horn shapes. However, as just discussed in the previous section the flowfields as seen in the oil flow visualization, and as described by the surface pressures, are different depending on the level of three-dimensionality in the ice shapes. That is whether the ice shape supports the formation of the leading-edge vortex or suppresses it. Thus, consistent with the philosophy of grouping ice shapes in consideration of the flow physics, these two different flowfields should be grouped into two different ice shape classifications. So, the horn classification now becomes:

- 3D leading-edge horn
- Highly 3D leading edge horn

Only a small number of shapes have been tested and the study of the flowfield physics is also limited. Thus, the understanding of the characteristics of these two classifications is not nearly complete. At this writing here is the best information for the critical characteristics of these two classifications based on the process depicted in Fig. 1. The 3D leading-edge horn ice shape classification is characterized by the horn size, location, and angle as in the 2D airfoil case. The variation and rate of change of this horn spanwise is small with respect to the size of the horn. The next section provides a summary of a small sensitivity study looking at these characteristics.

Providing characteristics of the highly 3D leading-edge horn is more difficult and uncertain. The location and size of the horn in a spanwise averaged sense is expected to be important to the flowfield and aerodynamics of the wing. The characterization of the rapid changes in the horn or ice shape spanwise is more difficult to characterize. Woodard et al.[17] have developed some basic parameters in studying the high-fidelity maximum scallop shape from this research program in an attempt to develop a simple, low-fidelity, representation of this shape. Tests of low-fidelity ice shapes based on these parameters for their aerodynamics are briefly summarized in the next section.

In summary, the proposed swept-wing ice shape characterization is:

- **Roughness:** key parameters are roughness height, location and density.
- **Streamwise:** key parameters are shape, roughness height and density
- **3D leading-edge horn:** key parameters are horn height, location, angle, and roughness
- **Highly 3D leading-edge horn:** key parameters are spanwise averaged are horn height, location, angle, spanwise variation of horn geometry, and roughness
- **Spanwise ridge:** key parameters are location and height

Tests of the one streamwise ice shape in this research program produced a type II flowfield for the high-fidelity shape and a type I flowfield for the 3D smooth low-fidelity version of this shape.[12,42] Thus, the argument could be made to remove streamwise ice from the classification and include this streamwise shape, and potentially all streamwise shapes, into the two new categories of horn shapes. Clearly, many streamwise shapes have a geometry that can be viewed as a horn shape on the leading edge oriented at a low angle roughly into the incoming relative wind. The authors have decided that one case was not enough to make this change - that other flowfield physics on additional examples of this shape may later suggest other classification solutions. For example, airfoil streamwise shapes have been tested that are very conformal to the leading edge which increases camber and effectively acts as a leading-edge device. Perhaps a future streamwise shape on a swept will also demonstrate these physics. So, for now the streamwise classification has been retained pending additional information in the future.

D. Parametric Studies of Swept Wing Ice Shape

Two studies were conducted as part of the Swept Wing Icing Research Program using simple ice shape geometries to better understand the sensitivity of ice shape parameters to aerodynamic performance. One set of shapes used simple horn geometries to better understand the 3D Horn swept wing ice shape classification in terms of horn size and angle. The second study explored ice shape geometry within the highly 3D horn geometry classification. These two studies are presented briefly below and much more information can be found in the references.

Horn ice sensitivity:

The 3D horn classification study considered horn size and angle. Much more information on this study can be found in Broeren et al.[42] The simple horn geometry was based on the WB33 ice shape. The icing conditions for this accretion case are shown in Table 1. In Fig. 23 the CAD renderings of the WB33 high-fidelity shape and the low-fidelity 3D smooth shape are shown as well as a simple 3D horn. These represent three very different fidelities of the same measured WB33 ice accretion.

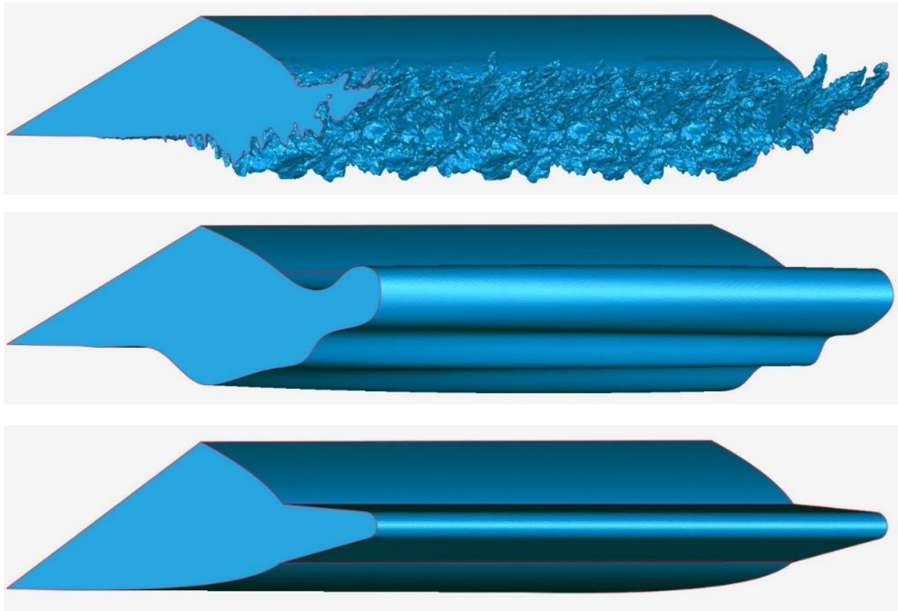

Fig. 23 Comparison of WB33 high-fidelity shape (top), 3D smooth shape (middle), and simple 3D horn (bottom) (Broeren et al.[42])

For the 3D horn sensitivity study two different horn heights and three different horn angles were tested. The horns were tested with two horn sizes of k/c = 0.0355 as shown in Fig. 23 and one half this horn height of k/c = 0.0177 as defined at the midspan. The horn angle measured from the chord line of 10 degrees is shown in Fig. 23. Horn angles of 25 degrees and 40 degrees were also tested. It should be noted that these simple horn shapes were not intended to match or accurately simulate the actual accreted ice geometry. Instead the horns were intended to be used to study the sensitivity of the aerodynamics to changes in horn size and angle ad be representative of horn parameters measured on actual accretions.

Remember that the swept-wing ice accretions are created based on measured accretions from the NASA IRT from three wind tunnel models each representing a different wing spanwise station.[43] Figure 24 shows the simple horns with 10 and 40-deg. angles and the two heights at the three spanwise stations compared to the WB33 3D smooth profiles and a LEWICE3D calculated shape.

Figure 25 shows the lift, pitching moment, and drag for the 10- and 25-deg ice horns at k/c = 0.0177 compared to the clean wing, and the wing with the 3D smooth shape and LEWICE3D shape. All of these were tested at Re = 2.4 x 10^6 and M = 0.026. All of these shapes show a much lower maximum lift, earlier moment break, and higher drag than the clean wing as expected. The lift and moment performance of the 10-deg horn compares well to the 3D smooth. Increasing the

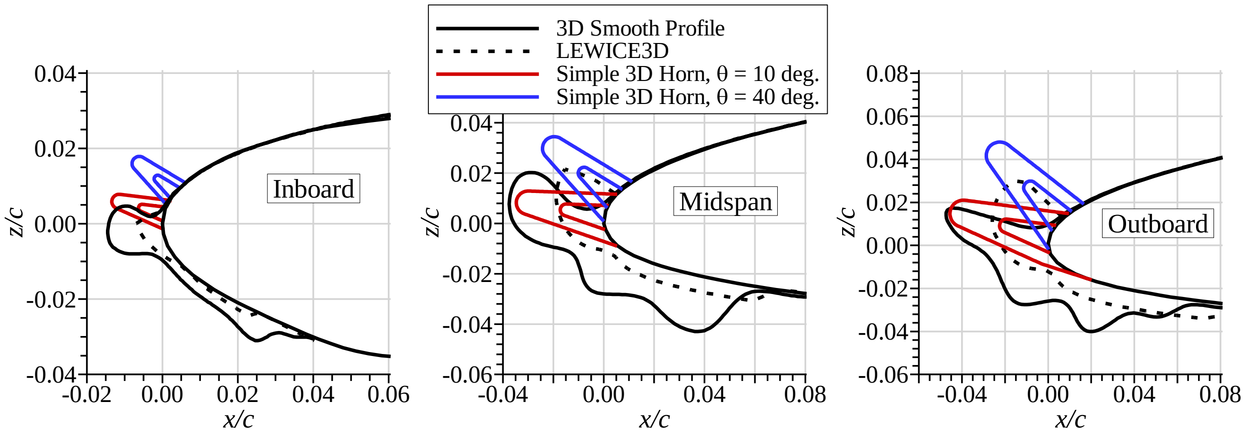

Fig. 24 3D smooth and LEWICE3D ice profiles compared to simple horn configurations at the three spanwise stations (Broeren et al.[42])

angle to 25 degrees produces a significant additional maximum lift penalty and earlier moment curve break. Thus, horn angle is shown here to have a significant effect on aerodynamic performance. The drag is more complex, but as expected the 25-deg. horn shape shows more drag at positive lift as compared to the 10-deg horn.

In Fig. 26 the maximum lift is shown versus Reynolds number for the 10-deg and 40-deg horns at the two heights and with grit. The grit indicates surface roughness at high density applied to the horn surfaces. The grit scales to a 3mm roughness at full scale. The first thing to note is that the change in C_{Lmax} with Reynolds number of 1.6 to almost 12 million is very small. No clear trend is seen (at least not above Re = $4x10^6$). With horn angle, however, the trend of reduced maximum lift with increasing horn angle from 10 to 40 degrees, is clear across all Reynold numbers. At a horn angle of 40 degrees, horn size has a clear effect on maximum lift with increasing size, decreasing maximum lift. The with horn angle of 10 degrees, the effect of roughness is less clear with almost no effect on maximum lift at the higher Reynolds numbers. The effect of horn angle and size on usable lift is also shown and follows the same trends, although more significant, Fig. 26. Similar sensitivity of the aerodynamics to horn length and angle has also been noted for airfoils. Note for example Fig. 5 where horns located s/c = 0.0 (also horns at a low angle to the flow, also saw reduced influence on maximum lift. Based on the more detailed results presented by Broeren et al.[42] these simple ice shapes have shown horn size and angle to be key parameters in understanding the 3D horn swept wing ice shape classification.

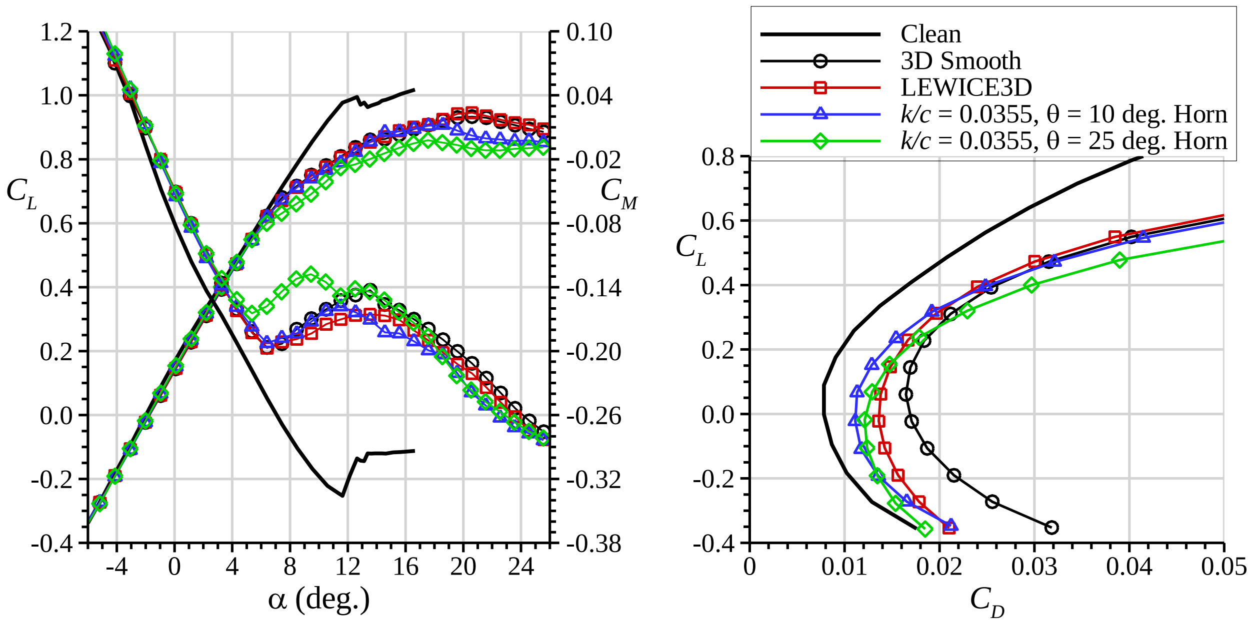

Fig. 25 Lift and moment performance of the swept wing including 3D simple horn shapes. Re = 2.4x10^6 and M = 0.026 (Broeren et al.[42])

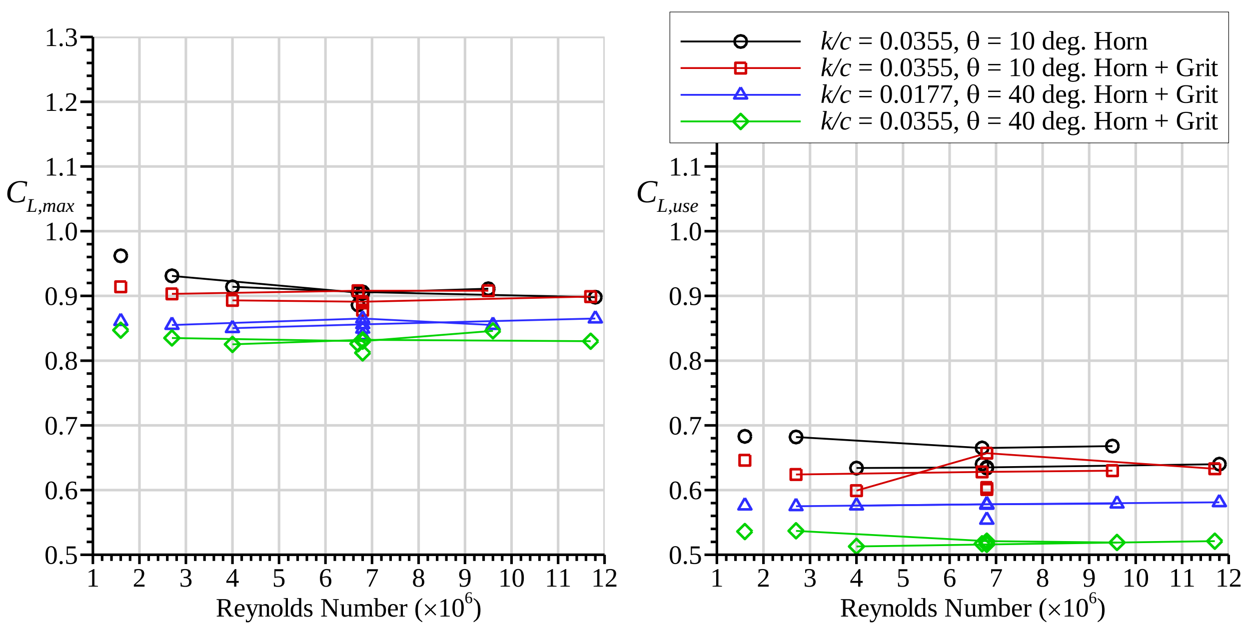

Fig. 26 Effect of Reynolds number on maximum lift and usable lift for swept wing including simple horn shapes (M = 0.09 to 0.34) (Broeren et al.[42])

Highly 3D Horn Ice*:*

Woodard et. al.[17,44] studied low-fidelity ice shape simulations of the maximum scallop ice shape. Three of these simulations are shown in Fig. 27. The first is the 3D smooth shape created by smoothing the maximum continuous cross-section. In aerodynamic testing of the 3D smooth and 3D smooth with grit, these low-fidelity simulations produced non-conservative lift and drag results compared to the high-fidelity simulation. To improve the simulation, and better understand the flowfield and overall aerodynamics, a simulation strategy was developed to produce a simple geometry that included some large variation of the geometry. The small gap discontinuous and medium gap discontinuous ice shapes were based on measurements of the scallops and the gaps that produce the streamwise vortices that have been shown to be important in the aerodynamics. The shapes were formed by including gaps in the 3D smooth shape as seen in Fig. 27. Other discontinuous configurations have been developed and tested but are not discussed here. [45]

The aerodynamics performance of the high-fidelity, small gap discontinuous and medium gap discontinuous is shown in Fig. 28. Here the lift and pitching moment are seen to be reasonably well predicted by both discontinuous shapes. Some discrepancy in the lift above eight degrees AoA and the moment between eight- and sixteen-degrees AOA exists but are relatively small. The drag is, however, not well predicted by the discontinuous shapes. Below $C_L = 0.3$ the drag is significantly under-predicted and above this value the drag is over-predicted by both discontinuous shapes. Oil flow visualization of the upper surface flow at AoA = 5.3 degrees is shown in Fig. 29. No evidence of a leading-edge vortex is seen in the oil flow of any of the three simulations. The high-fidelity clearly exhibits the oil streaks produced by the streamwise vorticity that is generated by the scallop geometry and that suppresses the leading-edge vortex formation (type II flow). The medium gap discontinuous shape also clearly shows this flowfield and, while harder to see in the flow visualizations because of the reduced size, the small gap discontinuous shape also has streamwise vorticity suppressing the leading-edge vortex.

The pressure distributions on the 6 streamwise pressure tap rows is shown in Fig. 30. All three simulations at all spanwise stations show the peaky leading-edge pressure distribution characteristic of the type II flowfield. At a higher angle of attack, not shown, the pressure agreement is not as good at all spanwise locations and especially near the Yehudi break. At these angles of attack the flowfield is not as clear and type I and II may both exist at different spanwise stations on the wing.

Much more analysis of this flowfield and the various low-fidelity simulations can be found in the literature.[17,44,45] The purpose of this paper, however, is swept wing ice shape classification, which includes identifying the critical geometric parameters and understanding the sensitivity of the aerodynamic performance to these parameters. (Thus, helping explore "how good is good enough.") For the highly 3D horn classification represented by the maximum scallop, it appears accurate modeling on lift and moment requires the large spanwise geometric variations like the discontinuous shapes tested. However, the drag is not well modeled and the flowfield modeling at all angles of attack (especially higher AoA) is not clear. It is not well understood at this time exactly how to characterize the parameters needed to characterize the simple shapes that can reliably capture all the physics in the large spanwise geometric variations seen in highly 3D horn ice on swept wings.

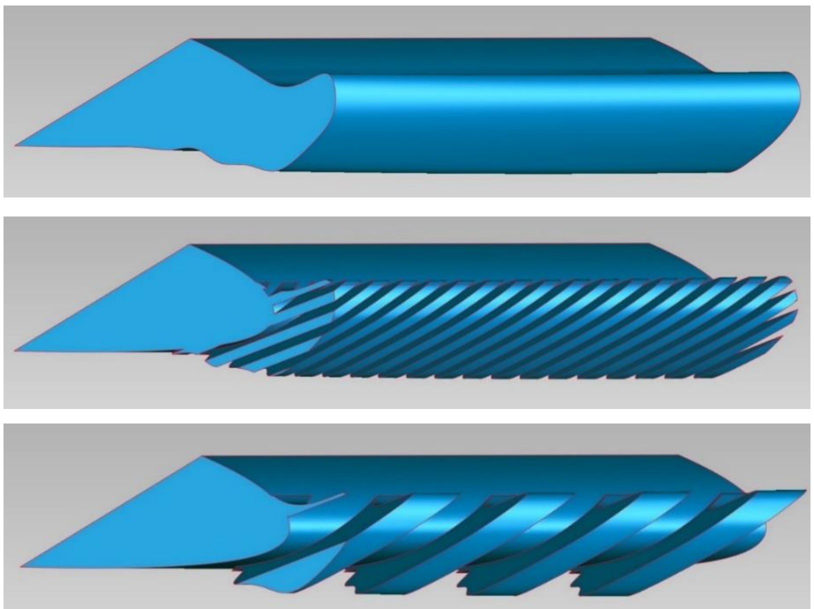

Fig. 27 Maximum Scallop 3D smooth (top), small gap discontinuous (middle), and medium gap discontinuous (bottom) low-fidelity ice shapes (Woodard et al.[44])

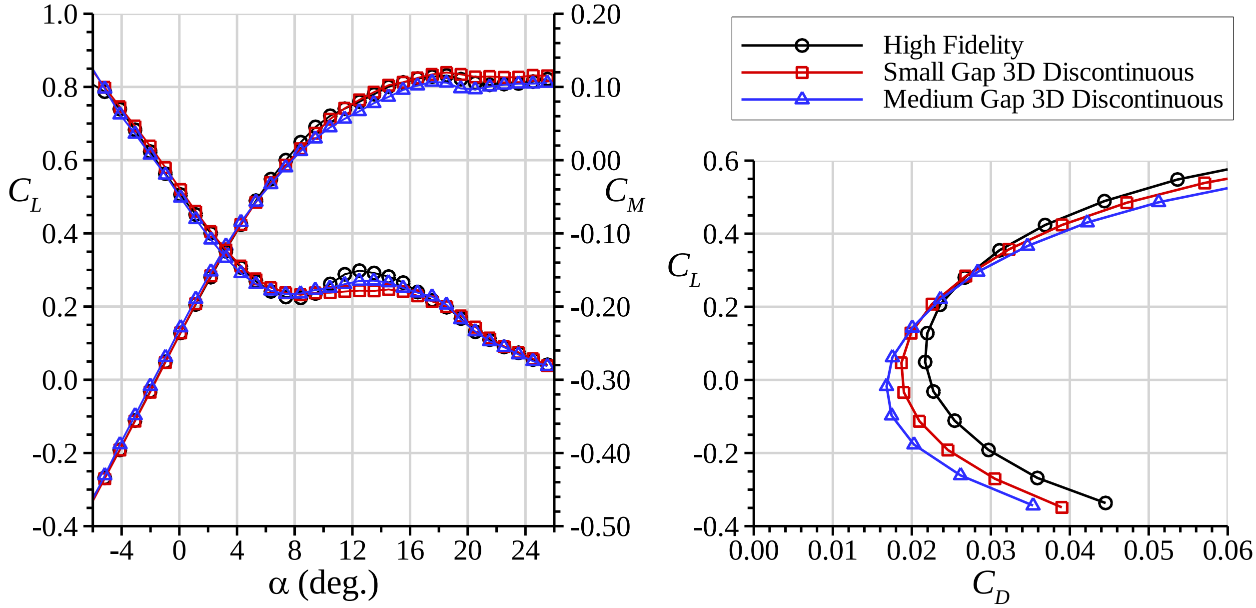

Fig. 28 Aerodynamic performance of high-fidelity max scallop and small and medium gap discontinuous ice shapes. Re = 1.6×10^6, M = 0.17

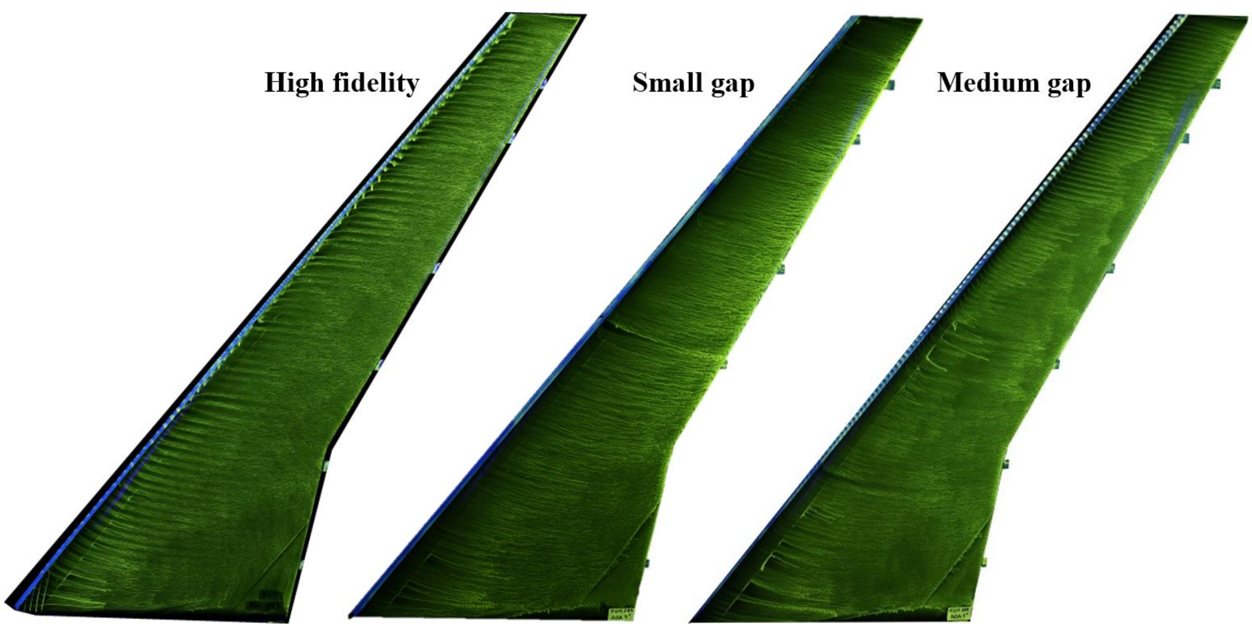

Fig. 29 Surface flow visualization for high-fidelity max scallop and small and medium gap discontinuous ice shapes. *Re* = 1.6×10^6, *M* = 0.17, AOA = 5.3

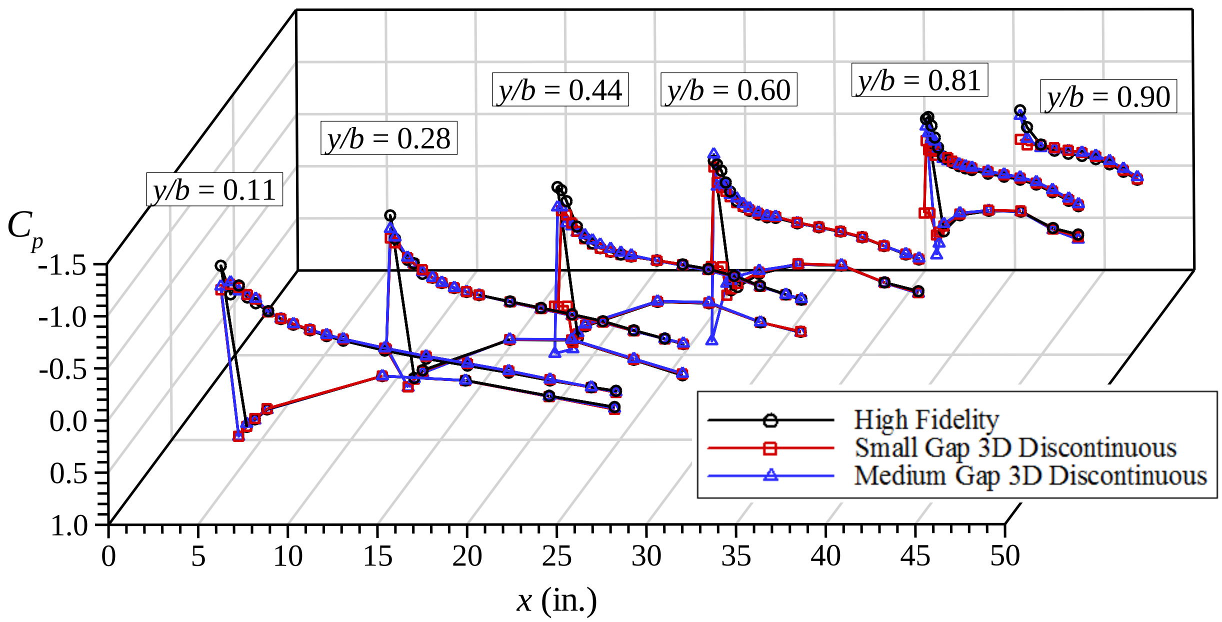

Fig. 30 Surface pressures for high-fidelity max scallop and small and medium gap discontinuous ice shapes. $Re = 1.6 \times 10^6$, $M = 0.17$, **AOA = 5.3**

E. Future Studies and Considerations

Iced Swept wing flow physics:

The 2D airfoil case had the advantage of years of more fundamental studies. Roughness flowfields about single elements and distributed roughness, fundamental transition and separation, backward-facing steps, and blunt flat plates had all been extensively studied and available in the literature. Some of these are noted in the review article of Bragg et al.[3]

To better interpret the current swept wing results additional flowfield and flow physics information is needed. Types of data that would be useful include off-body flow visualization, off-body flowfield velocities, and unsteady flowfield information. To better understand the type II flowfields it is especially important to document the flow through and around the scallop shapes and how this interacts with, and delays or prevents, the formation of the leading-edge vortex. This information will provide a better understanding of the flow physics and allow a better characterization of the ice shape geometry. With this information, researchers can provide simple geometries, low-fidelity simulations, and icing simulation code guidance, etc. to help contribute to “how good is good enough.”

Fundamental Flowfield studies:

For the airfoil horn ice case much was learned from fundamental experiments on laminar separation bubbles and backward-facing step flows. These fundamental experiments guided the researchers in more detailed examinations of the flow physics of the iced-airfoil flowfields and greatly contributed to the overall understanding of the flows.[3]

The iced swept wing case is comparable in some ways to the flow behind a swept, backward-facing step. This flow is characterized by the formation of a separated shear layer and recirculation vortex behind a sharp expansion, followed by reattachment. Due to the popularity of the 2D backward-facing step as a means of studying separating and reattaching flows, it is somewhat surprising that so few researchers have conducted detailed experimental and numerical studies of the swept backward-facing step. A significant portion of the papers offer insight into the effects of sweep angle rather than any geometric modifications of the step. This means that the literature offers little guidance towards the understanding of the spanwise discontinuities that are of primary interest in the scallop icing case. One exception is the paper focusing on the swept, backward-facing step conducted by Selby.[46] In addition to varying sweep angle and step height, Selby also made geometric modifications to the edge of the step, including shallow streamwise troughs that form counter-rotating vortices. This was the closest comparison to the spanwise variations seen in many of the previously discussed ice shapes. The experimental studies of the swept backward-facing step by Weber[47] acquired holt-film measurements while using Selby's experiments[46] as a benchmark. Similar to other studies, the direct numerical simulation results of Kaltenbach[48] investigated the effect of sweep and the independence principle between normal and spanwise flow behind the step. Kaltenbach and Janke[49] further studied the transitional flow over a swept step, again investigating the effect of sweep angle.

Yoshida[50] has undertaken an experimental study of a backward-facing step including discontinuous step geometry that is based on low-fidelity simulations of the scallop shapes of this research program.[17] The leading edge of a swept flat plate was fitted with a backward-facing step and also a discontinuous backward-facing step as shown in Fig. 31. Flow is from top to bottom on both Figs. 31 and 32. The Reynolds number based on a 0.5" step height was $5.11\text{x}10^4$ and the leading-edge sweep angle was 37.15 degrees matching that of the CRM wing leading edge. The plate spans the 36-inch width of the subsonic wind tunnel and is 64.2 inches long fitted with an additional 12" adjustable trailing-edge flap. Surface oil flow visualization, Fig. 32, on the backward-facing step (left image) clearly shows the leading-edge vortex and its reattachment just downstream of the leading edge. The lower right of the image shows the wall interference as it alters the leading-edge vortex. Secondary separation is seen as the oil flows forward and outboard toward the leading edge and then pools just downstream of the step. The distance the secondary separation is behind the step grows as the vortex moves outboard. The right image is the discontinuous step flow visualization. Here no spanwise vortex is seen and instead the streaks generated by the streamwise vorticity are present as seen in the highly 3D horn flow visualizations earlier in the paper.

In Fig. 33 the surface pressures are shown downstream of the step and the discontinuous step. In the notation of our earlier discussion, the solid backward-facing step exhibits a type I flowfield where the leading-edge vortex is present and the discontinuous backward-facing step shows a type II flowfield where the leading-edge vortex is suppressed. As seen earlier on the swept wing, the surface pressure is very different between the two cases. The backward-facing step sees a much lower pressure due to the separation and suction under the vortex. Here the minimum C_p is about -0.5 centered around 2 inches (4 step heights) downstream of the step. The discontinuous step doesn’t have an organized spanwise vortex, or the same acceleration of the flow over the step. For this case the peak negative pressure coefficient downstream of the step is -0.22 just downstream of the discontinuous step. Future studies plan to measure off body velocities and conduct off-body flow visualization to help better understand these flows.

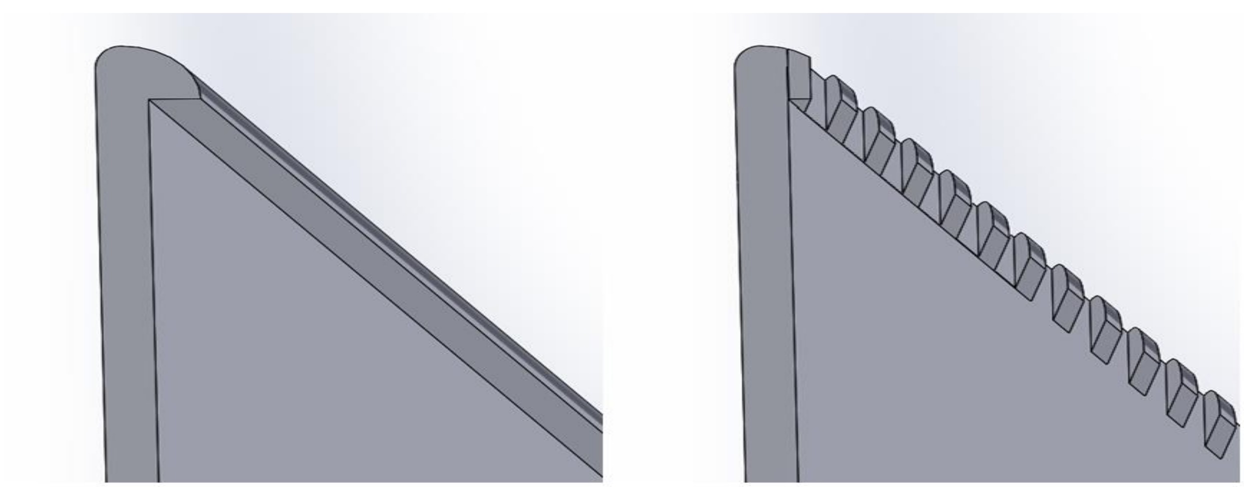

Fig. 31 Step leading-edge (left) and Discontinuous step geometries on a flat plate with leading-edge sweep angle of 37.15 degrees. (0.5” step height with step Re of $5.11x10^4$)

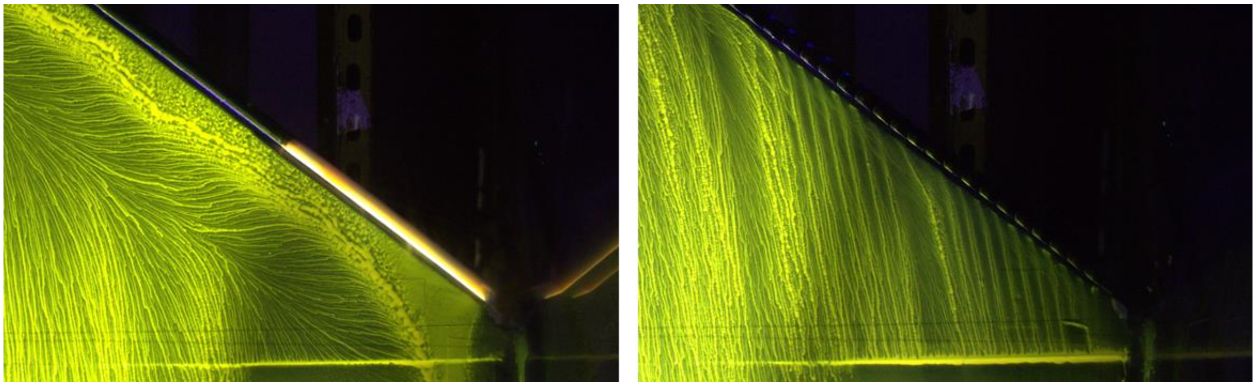

Fig. 32 Surface oil flow on swept plate with leading-edge step (left) and discontinuous step (right)

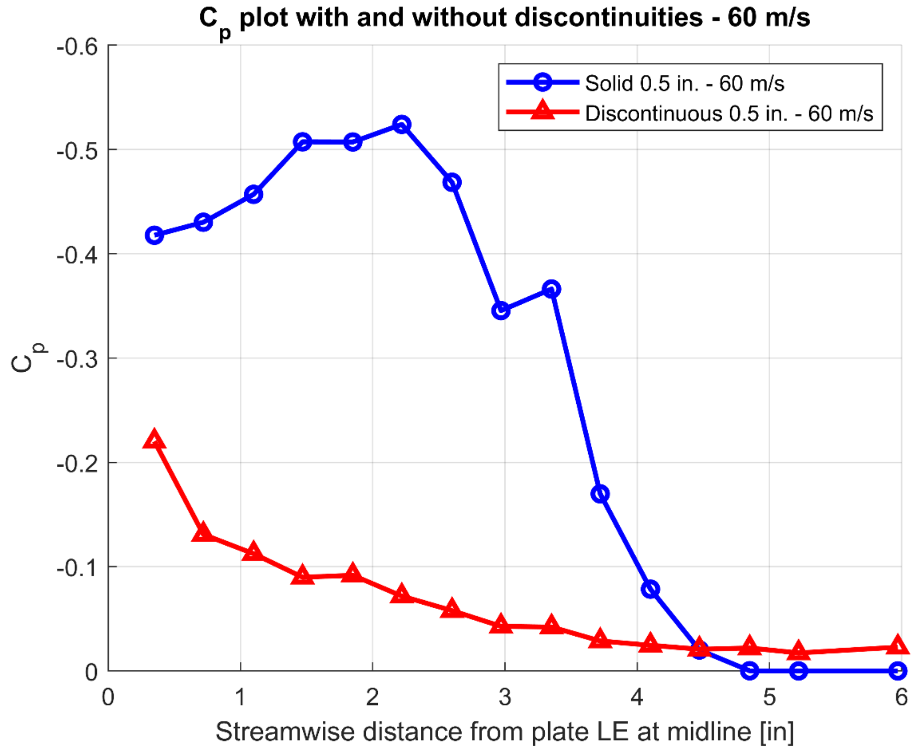

Fig. 33 Surface Pressure coefficient downstream of leading-edge step and discontinuous step on a swept plate leading edge

Effect of swept-wing geometry:

The research reported here used a CRM65 swept-wing configuration for the ice accretion and aerodynamics testing. This wing was highly tapered and twisted and included a Yehudi break.[51] The tested configuration had no engine or phylon, no flaps or control surfaces, and no tip devices. It is highly unlikely that any potential future engineering application of the data from this program or use of the ice shape classification system proposed here, will use this exact swept wing geometry. It was shown in Section II A) that the impact of airfoil design on the effect of horn ice shapes on the performance could be very significant. Swept-wing geometry is much more complex than 2D airfoil geometry and it can safely be assumed that the accretion and aerodynamic impact of ice accretion on a swept wing will be very dependent on the wing geometry. A simple example is the dependence of the leading-edge vortex on wing sweep.[21,22] The effect of ice accretion and ice accretion fidelity on the formation, or the delay in this formation, was shown as an important feature in the iced aerodynamic performance of this CRM65 wing. Wings of other sweep angles are expected to have different sensitivity to the leading-edge vortex formation and thus leading-edge ice shapes.

Lynch and Khodadoust[52] point out in their extensive review of aircraft and wing icing aerodynamics that the proper assessment of three-dimensional icing effects relies on an understanding of the spanwise variation in stall initiation on the clean wing. They note that 3D wings have a spanwise location that is critical to stall initiation. The addition of wing-mounted engines, nacelles and pylons can also modify the stall behavior. Therefore, it is important to know the critical section, span-load distribution, baseline wing stalling characteristics, and how ice accretion affects the stall progression relative to the critical section. All of this will vary from aircraft to aircraft and even with different aircraft configurations. Thus, while the ice shape classification proposed here is most likely to be valid across a variety of swept-wing geometries, the sensitivities of the aerodynamic performance will undoubtedly vary across different wing geometries. Hopefully the classification system and results presented here, and in the many other publications derived from this research, can help guide and inform determining "how good is good enough" for other geometries and configurations.

IV. Summary, Conclusions and Recommendations

This paper reviewed the concept and motivation for ice shape aerodynamic classification. The 2D airfoil classification that was developed in the mid-2000s is reviewed. The primary objective of this paper was to present new data and analysis to support an improvement to the swept-wing aerodynamic ice shape classification developed in 2013 based on the limited data available before the NASA/ONERA/FAA Sunset II swept wing icing program. For the swept-wing, two different flowfields are observed for different fidelities of the horn ice shapes representing scalloped ice accretion cases. These two cases represent different ice shape classifications that were not fully anticipated in the 2013 classification effort. The formation of a leading-edge separation vortex is a well-known flowfield for swept wings without leading-edge devices. Some high-fidelity horn ice shapes have highly-3D local geometric features (ice scallops) that produce a flowfield that delays the formation of this leading-edge vortex, referred to here as a Type II flowfield. Flow visualization suggests streamwise vorticity produced by the flow over and through the scallop geometry is a necessary feature of these flows. The lowest fidelity simulations that do not include the highly 3D features generate leading-edge vortices at lower angles of attack, referred to here as Type I flowfields. Surface roughness attached to low-fidelity shapes can in some cases result in Type II flowfields, particularly at low angles a of attack. Thus, it is proposed that the 2013 swept wing ice shape classification be updated to divide the horn classification into a 3D horn classification (generating primarily Type I flowfields) and a highly 3D horn classification (generating primarily Type II flowfields). The new proposed classifications are then:

- **Roughness:** key parameters are roughness height, location, and density.
- **Streamwise:** key parameters are shape, roughness height and density
- **3D leading-edge horn:** key parameters are horn height, location, angle, and roughness
- **Highly 3D leading-edge horn:** key parameters are spanwise averaged are horn height, location, angle, spanwise variation of horn geometry, and roughness
- **Spanwise ridge:** key parameters are location and height

The list above also includes the current best understanding of the key geometric parameters in each classification. These are important as they represent the key parameters that control the aerodynamic performance of the iced wing to the geometry of the ice shape in each classification. Thus, as is proposed in the paper, “how good is good enough” is best answered by providing the aerodynamics as a function of these parameters so "how good is good enough" can be determined for a specific application. In the recent data from this research program ice shapes in the streamwise, 3D horn and highly 3D horn ice classifications were tested. Limited tests were conducted using simple geometry and varying key geometric parameters to start to understand the sensitivity of the aerodynamics of the wing to these parameters. This included a 3D horn study varying horn size and angle, and also a study of discontinuous ice geometry to model highly 3D ice shapes unlike the 2D airfoil case where many of these studies have been conducted, our data set here is very limited. Thus, our understanding of the key parameters is at this time incomplete and more parametric studies, are needed. For the 3D horns more sizes and locations are needed including variations in size and angle with the spanwise location. For highly 3D horns, a better parameterization of the complex scallop geometry is needed. This should be facilitated by time-dependent off-body flowfield studies to better understand the relationship of the geometry to the flowfield. Also, some studies on at least one different swept wing geometry is needed to better understand how this affects the current results. As these additional data are acquired, and a better understanding of the flowfields and aerodynamics obtained, additional improvements to the ice-shape classifications for swept-wings are possible.

Acknowledgements

The authors wish to acknowledge the contributions of Mark Potapczuk, Tim Smith, James Riley, Chris Lum, Stephanie Camello, Jeff Diebold, Reza Soltani, and Kevin Ho who contributed in many ways from model design and construction, to wind tunnel testing and analysis, as well as many helpful discussions. The university authors were supported by FAA Grant Award Number 15-G-009. The FAA and ONERA also supported this research through interagency and international agreements, respectively. The NASA-supported portion of this research was originally funded under the Atmospheric Environment Safety Technologies Project of the Aviation Safety Program with continued support under the Advanced Air Transport Technology and Aeronautics Evaluation and Test Capabilities Projects of the Advanced Air Vehicles Program. These individuals, organizations, and projects are gratefully acknowledged.

References

[1] Broeren, A.P., Potapczuk, M.G., Riley, J.T., Villiedieu, P., Moens, F., and Bragg, M.B., "Swept-Wing Ice Accretion Characterization and Aerodynamics," AIAA Paper 2013-2824, June 2013, also NASA/TM—2013-216555, Sept. 2013.

[2] Broeren, A.P., Diebold, J.M., and Bragg, "Aerodynamic Classification of Swept-Wing Ice Accretion," NASA TM 2013-216381, DOT/FAA/TC-13/21, May 2013 and AIAA Paper 2013-2825.

[3] Bragg, M.B., Broeren, A.P., and Blumenthal, L.A., "Iced-Airfoil Aerodynamics," *Progress in Aerospace Sciences*, Vol. 41, No. 5, July 2005, pp. 323-418.

[4] Vargas, M., "Current Experimental Basis for Modeling Ice Accretions on Swept Wings," Journal of Aircraft, Vol. 44, No. 1, Jan.-Feb. 2007, pp. 274-290.

[5] Broeren, A.P., Potapczuk, M.G., Lee, S., Malone, A.M., Paul, B.P., Jr., and Woodard, B.S., "Ice-Accretion Test Results for Three Large-Scale Swept-Wing Models in the NASA Icing Research Tunnel," AIAA Paper 2016-3733, June 2016; also NASA/TM—2016-219137, Sept. 2016.

[6] Vassberg, J.C., DeHann, M.A., Rivers, S.M., and Wahls, R.A., "Development of a Common Research Model for Applied CFD Validation Studies," AIAA Paper 2008-6919, Aug. 2008.

[7] Rivers, M.B., and Dittberner, A., "Experimental Investigation of the NASA Common Research Model," AIAA Paper 2010-4218, June 2010.

[8] Rivers, M.B., and Dittberner, A., "Experimental Investigations of the NASA Common Research Model in the NASA Langley National Transonic Facility and the NASA Ames 11-Ft Transonic Wind Tunnel," AIAA Paper 2011-1126, Jan. 2011.

[9] Vassberg, J. C., Tinoco, E. N., Mani, M., Rider, B., Zickuhr, T., Levy, D.W., Brodersen, O., Eisfeld, B., Crippa, S., Wahls, R. A., Morrison, J. H., Mavriplis, D.J., and Murayama, M., "Summary of the Fourth AIAA CFD Drag Prediction Workshop," AIAA Paper 2010-4547, June 2010.

[10] Fujiwara, G. E., Woodard, B. S., Wiberg, B., Mortonson, A. J., and Bragg, M. B., "A Hybrid Airfoil Design Method for Icing Wind Tunnel Tests," *Proceedings of the 5th AIAA Atmospheric and Space Environments Conference*, AIAA Paper 2013-2826, San Diego, CA, June 2013.

[11] Broeren, A.P., Woodard, B.S., Diebold, J.M., and Moens, F., "Low-Reynolds Number Aerodynamics of an 8.9% Scale Semispan Swept Wing for Assessment of Icing Effects," AIAA Paper 2017-4372; also NASA/TM—2017-219533, July 2017.

[12] Camello, S.C., Bragg, M.B., Broeren, A.P., Lum, C.W., Woodard, B.S., and Lee, S., "Effect of Ice Shape Fidelity on Swept-Wing Aerodynamic Performance," AIAA Paper 2017-4373, June 2017.

[13] Lum, C.W., Sandhu, N., Diebold, J.M., Woodard, B.S., and Bragg, M.B., "The Application of a Five-Hole Probe Wake-Survey Technique to the Study of Swept Wing Icing Aerodynamics," AIAA Paper 2017-4374, June 2017.

[14] Broeren, A.P., Lee, S., Woodard, B.S., Lum, C.W., Smith, T.G., "Independent Effects of Reynolds and Mach Numbers of the Aerodynamics of an Iced Swept Wing," AIAA 10th Atmospheric and Space Environments Conference, Atlanta, GA, June 25-29, 2018.

[15] Lee, S., et al., "Comparison of Different Scale Model Iced Aerodynamics," AIAA 10th Atmospheric and Space Environments Conference, Atlanta, GA, June 25-29, 2018.

[16] Sandhu, N., Lum, C.W., Soltani, R., Bragg, M.B., "Effect of Artificial Ice Shape Fidelity on Iced Swept Wing Aerodynamics," AIAA 10th Atmospheric and Space Environments Conference, Atlanta, GA, June 25-29, 2018.

[17] Woodard, B.S., Broeren, A.P., Lee, S., Lum, C.W., and Bragg, M.B., " Summary of Ice Shape Geometric Fidelity Studies on an Iced Swept Wing," AIAA 10th Atmospheric and Space Environments Conference, Atlanta, GA, June 25-29, 2018, AIAA Paper 2018-3494

[18] Broeren, A.P., Lee, S., LaMarre, C.M., and Bragg, M.B., "Effect of Airfoil Geometry on Performance with Simulated Ice Accretions Vol. 1: Experimental Investigation." DOT/FAA/AR-03/64, Aug. 2003.

[19] Broeren, A.P., Addy, H.E., Jr., Bragg, M.B., Busch, G.T., Guffond, D., and Montreuil, E., "Aerodynamic Simulation of Ice Accretion on Airfoils," NASA/TP-2011-216929, June 2011.

[20] Busch, G.T., "Ice Accretion Aerodynamic Simulation on a Subscale Model, M.S. Thesis, Dept. of Aerospace Engineering, Univ. of Illinois, Urbana, IL, 2006.

[21] Poll, D.I.A., "Spiral Vortex Flow Over a Swept-Back Wing," Aeronautical Journal, May 1986.

[22] Furlong, G.C., and McHugh, J.G., "A Summary and Analysis of the Low-Speed Longitudinal Characteristics of Swept Wings at High Reynolds Number," NACA TR-1339, 1952.

[23] Neely, R.H, and Connor, D.W., "Aerodynamic Characteristics of a 42□ Swept-Back Wing With Aspect Ratio 4 and NACA 641-112 Airfoil Sections at Reynolds Numbers From 1,700,000 to 9,500,000," NACA RM L7D14, 1947.

[24] Koven, W., and Graham, R.R., "Wind-Tunnel Investigation of High-Lift and Stall-Control Devices on a 37□ Sweptback Wing of Aspect Ratio 6 at High-Reynolds Numbers," NACA RM L8D29, Sept. 1948.

[25] Van Hengst, J., Gent, R., Hammond, D., Seubert, R., and Wagner, B., "Ice Accretion and Its Effects on Aircraft," Paper 3 in "Ice Accretion Simulation" AGARD-AR-344, Dec. 1997.

[26] Papadakis, M., Yeong, H.W., Wong, S.C., Vargas, M., and Potapczuk, M.G., "Aerodynamic Performance of a Swept Wing With Ice Accretions," AIAA Paper 2003-0731, Jan. 2003.

[27] Papadakis, M., Yeong, H.W., Wong, S, Vargas, M and Potapczuk, M., "Experimental Investigation of Ice Accretion Effects on a Swept Wing," DOT/FAA/AR-05/39, Aug. 2005.

[28] Bragg, M.B., and Gregorek, G.M., "Wind Tunnel Investigation of Airfoil Performance Degradation Due to Icing," AIAA Paper 82-0582, Jan. 1982.

[29] Papadakis, M., Yeong, H.W., and Wong, S.C., "Aerodynamic Performance of a Swept Wing With Simulated Ice Shapes," AIAA Paper 2004-0734, Jan. 2004.

[30] Whalen, E.A. "Aerodynamics of Runback Ice Accretions," Ph.D. Dissertation, Dept. of Aeronautical and Astronautical Engineering, Univ. of Illinois Urbana-Champaign, Urbana, IL, 2007.

[31] Papadakis, M., and Gile-Laflin, B.E., "Aerodynamic Performance of a Tail Section with Simulated Ice Shapes and Roughness," AIAA Paper 2001-0539, Jan. 2001.

[32] Broeren, A.P., Whalen, E.A., Busch, G.T., and Bragg, M.B., "Aerodynamic Simulation of Runback Ice Accretion," AIAA Paper 2009-4261, Jun. 2009.

[33] Bragg, M.B., Kerho, M.F., and Khodadoust, A., "LDV Flowfield Measurements on a Straight and Swept Wing With a Simulated Ice Accretion," AIAA Paper 93-0300, Jan. 1993.

[34] Kwon, O.J., and Sankar, L.N., "Numerical Study of the Effects of Icing on Fixed and Rotary Wing Performance," AIAA Paper 91-0662, Jan. 1990.

[35] Khodadoust, A., and Bragg, M.B, "Measured Aerodynamic Performance of a Swept Wing With a Simulated Ice Accretion," AIAA Paper 90-0490, Jan. 1990.

[36] Papadakis, M., Alansatan, S., and Yeong, H.W., "Aerodynamic Performance of a T-tail With Simulated Ice Accretions," AIAA Paper 2000-0363, Jan. 2003.

[37] Papadakis, M., Yeong, H.W., Wong, S.C., Vargas, M., and Potapczuk, M.G., "Aerodynamic Performance of a Swept Wing With Ice Accretions," AIAA Paper 2003-0731, Jan. 2003.

[38] Papadakis, M., Yeong, H.W., Wong, S, Vargas, M and Potapczuk, M., "Experimental Investigation of Ice Accretion Effects on a Swept Wing," DOT/FAA/AR-05/39, Aug. 2005.

[39] Broeren, A.P., Lee, S., Woodward, B.S., and Bragg, M.B., "Effect of Geometric Fidelity on the Aerodynamics of a swept Wing with Glaze Ice Accretion," AIAA paper to be presented, June 2020.

[40] Lee, S., Broeren, A.P., Woodard, B.S., and Bragg, M.B., "Effect of Geometric Fidelity on the Aerodynamics of a Swept Wing with Scalloped Ice Accretion," AIAA Paper to be presented, June 2020.

[41] Diebold, J.M., private communication, April 2, 2020.

[42] Broeren, A.P., Potapczuk, M.G., Lee, S., Woodard, B.S. et al., "Experimental Aerodynamic Simulation of Glaze Ice Accretion on a Swept Wing," SAE Technical Paper 2019-01-1987, 2019.

[43] Camello, S.C., Lee, S., Lum, C.W., and Bragg, M.B., "Generation of Fullspan Leading-Edge 3D Ice Shapes for Swept-Wing Aerodynamic Testing," AIAA Paper 2016-3737, June 2016.

[44] Woodard, B.S., Broeren, A.P., Potapczuk, M.G., Lee, S., Lum, C.W., and Bragg, M.B, "Experimental Aerodynamic Simulation of a Scallop Ice Accretion on a Swept Wing." SAE Paper 2019-01-1984, June 2019.

[45] Woodard, B.S. and Bragg, M.B., "Effect of Spanwise Discontinuities on the Aerodynamics of a Swept Wing with Scalloped Ice Accretion," AIAA paper to be presented, June 2020.

[46] Selby, G.V., "Phenomenological Study of Subsonic Turbulent Flow Over a Swept Rearward-Facing Step," Ph.D. dissertation, Dept. of Mechanical and Aerospace Engineering, Univ. of Delaware, Newark, Delaware, 1982.

[47] Weber, D. J., "Hot Film Velocity Measurements Downstream of a Swept Backward-Facing Step," U.S. Army Chemical Research Development and Engineering Center, CRDEC-TR-221, Aug. 1990.

[48] Kaltenbach, H.-J., "Turbulent flow over a swept backward-facing step," European Journal of Mechanics - B/Fluids, vol. 23, 2004, pp. 501–518.

[49] Kaltenbach, H.-J., and Janke, G., "Direct numerical simulation of flow separation behind a swept, rearward-facing step at ReH=3000," Physics of Fluids, vol. 12, 2000, pp. 2320–2337.

[50] Yoshida, W., "Flowfield downstream of a Discontinuous Backward Facing step on a swept Flat Plat," M.S. Thesis, University of Washington, expected summer 2020.

[51] Vassberg, J.C., DeHann, M.A., Rivers, S.M., and Wahls, R.A., "Development of a Common Research Model for Applied CFD Validation Studies," AIAA Paper 2008-6919, Aug. 2008.

[52] Lynch, F.T., and Khodadoust, A., "Effects of Ice Accretions on Aircraft Aerodynamics," Progress in Aerospace Sciences, Vol. 37, No. 8, Nov. 2001, pp. 669-767.